Frontiers in Bioscience Landmark

Front. Biosci. (Landmark Ed) **2026**; 31(7): 51093
https://doi.org/10.31083/FBL51093

Original Research

Transcriptomic and Single-Cell Analyses Reveal a Prognostic Mitochondria- and Immunity-Related Risk Signature in Osteosarcoma

Jiangbo Ai[1,2,†], Zhidong Peng[1,2,†], Peichuan Xu[1,2], Jinghong Yuan[1,2], Xinxin Miao[1,2], Guoyu Yang[1,2], Jiangminghao Zhao[1,2], Xigao Cheng[1,2,*]

[1]Department of Orthopaedics, The Second Affiliated Hospital, Jiangxi Medical College, Nanchang University, 330006 Nanchang, Jiangxi, China
[2]Jiangxi Provincial Key Laboratory of Spine and Spinal Cord Disease, Nanchang University, 330006 Nanchang, Jiangxi, China
*Correspondence: xigaocheng@hotmail.com (Xigao Cheng)
[†]These authors contributed equally.
Academic Editor: Elisa Belluzzi
Submitted: 18 February 2026 Revised: 5 June 2026 Accepted: 12 June 2026 Published: 27 July 2026

Abstract

Background: While mitochondrial dysfunction and immune cell dysregulation have been established as important contributors to the pathogenesis of osteosarcoma (OS), the prognostic value of mitochondria-related genes (MRGs) and immune-related genes (IRGs) in OS remains poorly understood. **Methods:** Data were obtained from public databases. Differentially expressed genes (DEGs) and key module genes were identified viadifferential expression analysis and weighted gene co-expression network analysis, respectively. Candidate genes of interest were identified by intersecting key module genes, DEGs, MRGs, and IRGs. Then, candidate genes were screened using regression analysis and proportional hazards assumption testing to identify prognostic genes. A risk model was then constructed in the TARGET-OS dataset and validated in GSE16091. Independent prognostic, immune infiltration, and gene expression analyses were conducted. In addition, single-cell analysis was performed to identify key cell populations, and pseudotime analysis as well as cell communication network construction were carried out. Finally, the expression patterns of selected prognostic genes were additionally validated via reverse transcription quantitative polymerase chain reaction (RT-qPCR), and the functional role of protein kinase Cα (*PRKCA*) in osteosarcoma cell proliferation, migration, and invasion was evaluated *in vitro*. **Results:** Glutathione S-transferase Pi-1 (*GSTP1*), catalase (*CAT*), *TNFSF10*, and *PRKCA* were identified as mitochondria- and immunity-related prognostic genes in OS and were used to construct a risk model. The risk model was able to effectively predict the survival of patients with OS. A nomogram based on the identified prognostic genes additionally exhibited excellent performance when predicting OS patient survival. Significant differences in the abundance of 14 immune cell types and 8 immune checkpoint molecules were noted between the high-risk and low-risk groups. Single-cell analyses were then conducted to annotate 10 cell types, and M1 macrophages were identified as a potentially relevant cell population in the OS microenvironment. During M1 macrophage differentiation, initial reductions in *CAT* and *PRKCA* expression were noted, followed by subsequent increases and final decreases. In contrast, the expression of *GSTP1* and *TNFSF10* in these cells first rose and then declined. Furthermore, *PRKCA* was selected for further *in vitro* analyses, which revealed that it can enhance the invasion, migration, and proliferation of OS cells. **Conclusion:** This study identified *GSTP1*, *CAT*, *TNFSF10*, and *PRKCA* as prognostic genes associated with mitochondrial and immune function in OS, with *in vitro* evidence providing direct support for the potential functional role of *PRKCA* in OS progression. These findings highlight a new avenue for predicting clinical prognosis in OS and may provide a basis for future studies of putative therapeutic targets.

Keywords: osteosarcoma; mitochondrial-related genes; immune-related genes; nomogram; single-cell analysis; prognostic genes

1. Introduction

Osteosarcoma (OS) is the most common primary bone malignancy and mainly affects children and young adults, and is characterized by rapid progression and poor survival [1]. Significant improvements in OS patient prognosis have been achieved through advances in chemotherapy, surgical resection, and immunotherapy. However, the prognosis of patients with metastatic or recurrent OS remains unsatisfactory, with a 5-year survival rate for patients with lung metastases remaining lower than 20% [2,3,4]. Grade III lesions have the highest rate of local recurrence and an extremely poor prognosis, with 50% of affected patients developing lung metastases [5]. Even after successful treatment, chemotherapy and surgical treatment for osteosarcoma may cause long-term adverse effects, such as cardiotoxicity and nephrotoxicity, which can seriously affect patients' quality of life [6,7]. There is thus a pressing need to identify reliable prognostic genes and novel therapeutic targets to guide the more effective prediction, detection, and management of OS.

Mitochondria actively regulate tumor anabolic activity, modulate redox and calcium homeostasis, control transcription, and shape the induction or inhibition of cell death. Mitochondrial dysfunction can lead to cytochrome C release, the production of mitochondrial reactive oxygen species (ROS), and metabolite generation, propagating sig-

naling cascades that alter gene expression, cell activation, cell proliferation, and differentiation [8,9]. Mitochondrial pathways also play key roles in the onset and progression of OS. For instance, Toki et al. [10] found that the formation of the mitochondrial BIG3–PHB2 complex affects the survival and proliferation of OS cells. Lai et al. [11] further characterized a close association between mitochondria-related cell death and energy metabolism in OS cells. Dysregulated immune cell activity has also been identified as an important driver of malignant activities in OS [12]. Notably, Wang et al. [13] established innate immune cells as potential cellular targets for the treatment of OS. Tumor-associated macrophages are the most abundant infiltrating cell type found in the OS immune microenvironment and play an important role in matrix remodeling, inflammation, angiogenesis, immune defense, and regulation [14]. In addition to their bioenergetic importance, mitochondria play broad regulatory roles in mammalian immunity, with mitochondrial biosynthesis, fusion, and fission all shaping the activation and function of immune cells [15]. Intriguingly, recent studies have documented the ability of mitochondria to be transferred from immune cells to tumor cells through physical nanotubes that allow them to provide energy to tumor cells. This nanotube-mediated mitochondrial hijacking mechanism can facilitate immune evasion, highlighting it as a promising new target for cancer immunotherapy [16]. Current evidence thus delineates the tightly interrelated functions of mitochondria, immunity, and tumors [17]. Despite this understanding, most studies to date evaluating mitochondria and immunity in the context of OS have focused on individual factors without any systematic analysis. The comprehensive analysis of the prognostic relevance and functional importance of mitochondria-related genes (MRGs) and immune-related genes (IRGs) thus offers new opportunities for OS diagnosis and treatment.

Given the importance of mitochondrial function and immune characteristics in the onset and progression of OS, this study was designed with the goal of identifying prognostic MRGs and IRGs in this cancer type, establishing a risk model for predicting OS patient prognosis, and analyzing the biological functions of prognostic genes and their relationships with clinical characteristics, the immune microenvironment, immunotherapy response, and drug sensitivity. The overall goal of this approach is to establish an effective means of predicting the prognosis of OS patients and guiding the care of affected individuals.

2. Materials and Methods

2.1 Data Extraction

The TARGET database (https://ocg.cancer.gov/programs/target) was used to obtain RNA-seq and clinical data for the TARGET-OS dataset, which consists of 88 OS tissue samples. After excluding 3 samples with incomplete gene expression or survival data, a total of 85 patients were ultimately included in the risk model construction. A risk model was constructed using the $\log_2$-normalized TPM expression matrix extracted from this dataset. Ensembl IDs were converted into gene symbols by combining them with the corresponding species-specific annotation files. The Gene Expression Omnibus database (http://www.ncbi.nlm.nih.gov/geo/) was used to obtain the GSE36001 (GPL6102), GSE16091 (GPL96), and GSE162454 (GPL24676) datasets. The GSE36001 dataset comprised 19 OS samples and 6 control samples (osteoblasts and bone tissue), while the GSE16091 validation dataset comprised 34 OS tissue samples with complete patient survival information and gene expression data, and the GSE162454 single-cell dataset comprised 6 OS tumor tissue samples. A total of 2030 MRGs were identified by searching for the keyword "mitochondria" in the MitoCarta 3.0 (https://www.broadinstitute.org/mitocarta/mitocarta30-inventory-mammalian-mitochondrial-proteins-and-pathways) and Gene Set Enrichment Analysis (GSEA) databases (https://www.gsea-msigdb.org/gsea/index.jsp) [18]. In addition, 2660 IRGs were identified based on a review of the published literature [19].

2.2 Weighted Gene Co-Expression Network Analysis (WGCNA)

Using OS as a phenotype, a WGCNA approach was implemented [20] on the sample expression matrix in the GSE36001 dataset using the WGCNA package (v 1.71, Los Angeles, CA, USA). First, all samples were clustered, and hierarchical clustering was performed using the Euclidean distance based on expression levels to identify and eliminate potential outliers. Then, the optimal soft threshold was determined to ensure that the constructed network exhibited a scale-free topology. Subsequently, a scale-free network was constructed by applying the optimal soft threshold, resulting in the division of genes into multiple modules. The screening criteria included a minimum gene count per module of 500, a shear tree parameter of 4, and a module merging parameter of 0.25. Correlation coefficients corresponding to the relationships between modules and phenotypes were then computed to identify modules significantly associated with OS ($|\text{correlation (cor)}| > 0.4$, $p < 0.05$), and the genes within those modules were considered key module genes.

2.3 Differential Expression Analysis

Using the limma package (v 3.54.0, Melbourne, Victoria, Australia) [21], differentially expressed genes (DEGs) were screened when comparing the OS and control groups in the GSE36001 dataset based on the following screening criteria: $p < 0.05$ and $|\log_2 \text{fold change } (\log_2 FC)| > 0.5$. DEG distributions were assessed by generating volcano plots using the ggplot2 package (v 3.4.4, Boston, MA, USA) [22], while the ComplexHeatmap package (v 2.14.0, Heidelberg, Baden-Württemberg, Germany) [23] was used to create an expression heatmap of 20 DEGs.

2.4 Enrichment Analysis and Protein–Protein Interaction (PPI) Network Construction

To identify those DEGs associated with both mitochondria and immunity in OS, the overlap among key module genes, DEGs, MRGs, and IRGs was visualized to obtain candidate genes for subsequent analysis using the VennDiagram package (v 0.1.9, Los Angeles, CA, USA) [24]. The clusterProfiler package (v 4.7.1.003, Guangzhou, China) [25] was then used to perform Gene Ontology (GO) function and Kyoto Encyclopedia of Genes and Genomes (KEGG) enrichment analyses for candidate genes ($p < 0.05$). To further elucidate the protein-level interactions among these candidate genes, the STRING database (https://string-db.org/) was queried with an interaction score threshold of >0.4. The network was then visualized with Cytoscape (v 3.9.1, La Jolla, CA, USA) [26].

2.5 Construction of the Risk Model

Using the survival package (v 3.5-3) [27], candidate genes associated with OS prognosis were screened via univariate Cox regression analysis ($p < 0.2$). Those genes associated with OS patient prognosis were sequentially included in the proportional hazards (PH) hypothesis test ($p > 0.05$) and least absolute shrinkage and selection operator (LASSO) regression analysis, the latter of which was implemented using the glmnet package (v 4.1-4, Stanford, CA, USA) (https://CRAN.R-project.org/package=glmnet). Those genes remaining following LASSO regression were defined as prognostic genes and retained for subsequent analysis.

A risk model was established based on the prognostic genes obtained via LASSO regression. The linear coefficient obtained by LASSO regression was used as the coefficient, and this risk score was calculated as follows: risk score = $\sum_{i=1}^{n}(\beta_i \times Expr_i)$, where β_i and $Expr_i$ represent the LASSO regression coefficient and relative expression of each prognostic gene, respectively. Subsequently, patients with OS in the TARGET-OS dataset were divided into high- and low-risk subgroups based on the optimal risk score cutoff. Kaplan–Meier (KM) survival analysis was employed to compare differences in survival between the two risk subgroups using the survminer package (v 0.4.9, Dakar, Dakar Region, Senegal) [28]. In addition, the survivalROC package (v 1.0.3, Seattle, WA, USA) [29] was utilized for receiver operating characteristic (ROC) curve generation. The risk curve and survival status map were applied to illustrate the distribution of samples within the two risk cohorts, whereas a heatmap was constructed to visualize the expression patterns of prognostic genes between these cohorts. The performance of the risk model was additionally validated using KM survival, ROC curve, risk curve, and survival status analyses in the GSE16091 dataset. Internal validation of the model's discriminative ability on both the TARGET-OS and GSE16091 datasets was performed using 1000 bootstrap resampling iterations.

2.6 Independent Prognostic Analysis

Factors independently associated with OS patient prognosis were identified through sequential univariate Cox regression analysis ($p < 0.05$), PH hypothesis testing ($p > 0.05$), and multivariate Cox regression analysis ($p < 0.05$) evaluating risk scores, sex, age, and stage. Then, a nomogram was constructed using the identified independent prognostic factors to predict the 3-, 5-, and 7-year survival probabilities of patients with OS. Calibration curves and decision curve analysis (DCA) were next conducted to evaluate the predictive power of the established nomogram. Two Cox regression models were constructed for this study: Model A, which included sex, age, and disease stage, and Model B, which included sex, age, stage, and prognostic genes. Model performance was evaluated based on factors including the concordance index (C-index), ROC curve analysis, and DCA.

2.7 Clinical Stratification Analysis

To further investigate the relationships between clinical characteristics and risk score values, differences in risk scores between different subgroups with different clinical characteristics in the TARGET-OS dataset were explored using Wilcoxon's test. To assess differences in survival between the two risk cohorts based on differing clinical characteristics, KM survival analyses were conducted.

2.8 Enrichment Analysis Between the Two Risk Cohorts

The DESeq2 package was used to identify DEGs between the risk cohorts in the TARGET-OS dataset ($adj.p < 0.05$ and $|\log_2 FC| > 1$). Then, GO and KEGG enrichment analyses of the identified DEGs were performed using the clusterProfiler package. The obtained genes were sorted in descending order based on $\log_2 FC$ values, followed by GSEA, using the c2.cp.kegg.v7.5.1.symbols.gmt gene set from the Molecular Signatures Database (MSigDB) as the reference. In addition, the Gene Set Variation Analysis (GSVA) package (v 1.46.0, Barcelona, Catalonia, Spain) was used to explore differences in prognostic genes enriched in relevant pathways between the two risk cohorts, with c5.go.v7.4.symbols.gmt from MSigDB serving as the background gene set.

2.9 Exploration of the Immune Microenvironment

Immune cell infiltration was analyzed in the TARGET-OS dataset using the single-sample GSEA algorithm from the GSVA package (v 1.46.0) [30], followed by Wilcoxon's test to compare the differences in the extent of immune cell infiltration between the two risk subgroups. The expression of common immune checkpoints was additionally compared between the two risk subgroups [31]. Correlations between differential immune checkpoints and prognostic genes were additionally analyzed via Spearman's correlation analysis. The ESTIMATE algorithm was also used to compute the stromal, immune, and ESTIMATE scores for each sample.

2.10 Drug Sensitivity Analysis

The half-maximal drug inhibitory concentration (IC_{50}) values for 138 drugs and 3 commonly used chemotherapeutic drugs employed in the treatment of OS (methotrexate, doxorubicin, and cisplatin) were obtained in the TARGET-OS dataset using the oncoPredict package (v 0.2, Minneapolis, MN, USA) [32] in the Genomics of Drug Sensitivity in Cancer database (https://www.cancerrxgene.org/). Immediately thereafter, the psych package (v 2.2.9, Evanston, IL, USA) [33] was employed to perform Spearman's correlation analysis to compare the correlations between the IC_{50} values for these drugs and risk scores based on the following significance thresholds: $|R| > 0.3$ and $p < 0.05$. Then, the IC_{50} values of common chemotherapeutic agents were compared between the two risk cohorts.

To investigate the potential regulatory patterns of prognostic genes, the miRanda database (https://tools4mirs.org/software/target_prediction/miranda/) and the MicroRNA Target Prediction Database (miRDB, https://mirdb.org/) in the multiMiR package (v1.20.0) were used to predict upstream microRNAs (miRNAs) of the prognostic genes. The regulatory interaction pairs obtained from the two databases were intersected to identify the target miRNAs. Subsequently, the Encyclopedia of RNA Interactomes (starBase) database (https://rnasysu.com/encori/) was used to predict upstream long noncoding RNAs (lncRNAs) of the target miRNAs. Finally, the ggraph package (v2.1.0) was used to construct the lncRNA–miRNA–mRNA regulatory network.

2.11 Single-Cell Analysis

Using the GSE162454 dataset, we explored prognostic gene expression in tissue samples from patients with OS at the single-cell level using the Seurat package (v 4.3.0, New York, USA) [34] to create single-cell data as Seurat objects. The single-cell data were initially subjected to quality-control measures to identify high-quality cells, characterized by gene counts ranging from 200 to 10,000 per cell and a mitochondrial ratio lower than 10%. Then, the LogNormalize function was employed to normalize the feature expression measurements in each cell by dividing them by the total expression, after which values were multiplied by a scaling factor (default = 10,000) and the results were subject to logarithmic transformation. The FindVariableFeatures function was utilized for filtering, selecting only the top 2000 highly variable genes after quality control as significant features. Linear dimensionality reduction was then applied to obtain an optimal linear dimension value for cell clustering and subsequent classification of these cell clusters. Additionally, principal component analysis (PCA) was conducted to evaluate the distribution of OS and control samples. Subsequently, marker genes were obtained using findings reported in the literature [35]. Cell groups were precisely annotated to identify specific cell types, and the resulting annotations were visualized using Uniform Manifold Approximation and Projection. Finally, we evaluated the expression of prognostic genes at the cellular level. Annotated cells with higher expression levels for prognostic genes were defined as critical cells, and the key cells were clustered twice. The ReactomeGSA package (v 1.12.0, Vienna, Vienna, Austria) [36] was used for functional enrichment analyses of these key genes to explore signaling pathways related to OS progression.

2.12 Pseudotime and Cellular Communication Analyses

To more fully understand the changes in prognostic gene expression during cell differentiation, the Monocle package (v 2.26.0, Seattle, WA, USA) [37] was applied for pseudotime analysis of key cells. After acquiring the pseudotime information for these cells, the prognostic genes were included in a pseudotime analysis, visualizing their expression in key cells. Finally, cellular interactions were explored using the CellChat Database (https://github.com/jinworks/CellChat) with CellChatDB.human as a reference. The CellChat package (v 1.6.1, San Francisco, CA, USA) [38] was used to conduct communication analyses of all cell types and to map cellular interaction networks and ligand–receptor interaction networks, thereby yielding the number and strength of communication networks.

2.13 Analysis of Prognostic Gene Expression

Wilcoxon's test was used to analyze the differential expression of prognostic genes in OS samples from the GSE36001 dataset. The results were subsequently visualized by plotting box plots using the ggplot2 package.

2.14 OS Cell Culture and Treatment

Human osteoblasts (HFOB1.19) and human OS cell lines (HOS and U2OS) were obtained from the American Type Culture Collection (https://www.atcc.org) and maintained in our laboratory for further culture. All cell lines were authenticated by the supplier, and confirmed to be negative for mycoplasma contamination. Cell validation was performed by short tandem repeat (STR) profiling to verify cell identity, and PCR-based mycoplasma detection was carried outregularly to rule out contamination. HOS cells were cultured in Minimum Essential Medium (Thermo Fisher Scientific, Waltham, MA, USA) supplemented with 10% fetal bovine serum (FBS; Thermo Fisher Scientific) and 1% penicillin–streptomycin (Solarbio, Beijing, China) in a humidified 5% CO_2 incubator at 37 °C. HFOB1.19 and U2OS cells were maintained in Dulbecco's modified Eagle's medium containing the same supplements in a humidified 5% CO_2 incubator at 37 °C. To suppress protein kinase Cα (*PRKCA*) expression, Ribobio (Guangzhou, China) synthesized specific siRNA and corresponding negative control constructs. Transfection was conducted using the Ribofect CP transfection reagent (Ribobio) according to the manufacturer's instructions. Lentiviral particles were provided by Genechem (Shanghai, China).

2.15 RNA Extraction and RT-qPCR

Total RNA was extracted from cells or tissue specimens using TRIzol reagent (Thermo Fisher Scientific) and chloroform (Thermo Fisher Scientific). The extracted RNA was reverse-transcribed using the PrimeScript RT Kit (TaKaRa, Kyoto, Japan) to generate the corresponding cDNA, which served as the template for RT-qPCR amplification using specific primers **(Supplementary Table 1**).

2.16 Cell Counting Kit-8 (CCK-8) Assay

A CCK-8 assay was used to evaluate cell viability and proliferative capacity. Cells were seeded into 96-well plates containing complete medium at a density of 1500 cells per well and cultured in a humidified 5% CO_2 incubator at 37 °C. At 24, 48, and 72 h after seeding, 10 µL of CCK-8 reagent was added per well, and the plates were incubated for an additional 1–2 h. Absorbance was then measured at 450 nm using a microplate reader at each time point.

2.17 Wound Healing Assay

Cell migration was evaluated using a scratch wound healing assay. Briefly, approximately 5×10^5 cells were seeded into each well of a 6-well plate and incubated until approximately 90% confluent. A linear scratch was then introduced into the monolayer using a sterile 10-µL pipette tip. Dislodged cells were removed by washing twice with PBS, after which the remaining cells were cultured in serum-free medium. Images of the scratched region were acquired at 0 and 24 h post-scratching using a phase-contrast microscope.

2.18 Transwell Assay

To evaluate the invasive and migratory potential of OS cells, we performed Transwell invasion and migration assays. After preparing cells at 5×10^5 cells/mL, a 200 µL volume of the prepared cell suspension was added to the upper chamber of a Transwell insert precoated with Matrigel (Corning, Corning, NY, USA). The lower chamber was filled with 700 µL of medium supplemented with 10% FBS. The assembled Transwell chambers were incubated at 37 °C for 48 h in a humidified 5% CO_2 incubator. Following incubation, noninvading cells on the upper surface of the membrane were gently removed using cotton swabs. Cells that had invaded through the membrane to the lower surface were fixed with 4% paraformaldehyde for 15 min and subsequently stained with 0.1% crystal violet (Solarbio; G1064) for 20 min. Finally, stained cells were observed and counted under an inverted microscope at ×100 magnification across five randomly selected fields of view.

2.19 Western Blotting

Cells were washed three times with PBS and lysed using RIPA lysis buffer (Servicebio, Wuhan, China) for protein extraction, after which protein concentrations were determined using a BCA assay kit. Protein samples were separated by SDS-PAGE and transferred onto polyvinylidene fluoride (PVDF) membranes (MilliporeSigma, Burlington, MA, USA). After blocking with 5% skim milk, membranes were incubated overnight at 4 °C with a primary antibody against *PRKCA* (1:5000). After three washes with TBST, membranes were incubated with a secondary antibody and visualized for band detection.

Biological replicates refer to independent experiments performed using different animals, different biological samples, or independently cultured cell batches, whereas technical replicates refer to repeated measurements of the same sample. Unless otherwise stated, the statistical analyses were based on biological replicates.

2.20 Statistical Analysis

All data were analyzed using R software (v 4.2.2, R Foundation for Statistical Computing, Vienna, Austria). The Wilcoxon test was utilized to assess differences between the groups. Hazard ratios (HRs) and 95% confidence intervals (CIs) were calculated for univariate and multivariate Cox regression analyses. For KM survival analyses, survival differences between groups were evaluated using the log-rank test, and HRs with 95% CIs were estimated using Cox PH models. Time-dependent ROC curves were used to evaluate the predictive performance of the prognostic model. The area under the curve (AUC) values were reported with 95% CIs where applicable. The C-index and bootstrap-corrected C-index were calculated, and 95% CIs were estimated using 1000 bootstrap resampling iterations. A two-sided $p < 0.05$ was considered significant.

3. Results

3.1 Identification of 15,177 Key Module Genes and 2345 DEGs

WGCNA was implemented to identify OS-related module genes. Clustering results indicated that the GSE36001 dataset was free of outliers such that all samples were retained for the subsequent analysis (Fig. 1A). A soft threshold value of five was determined to be optimal, based on an R^2 of 0.971 and a connectivity of close to 0 (Fig. 1B), allowing for the identification of nine gene modules (Fig. 1C). Of these modules, MEturquoise, MEyellow, MEblack, MEblue, MEbrown, and MEgreen were significantly correlated with OS ($|cor| > 0.4$, $p < 0.05$). The integration of the genes from these modules yielded 15,177 key module genes (Fig. 1D). Differential expression analysis implemented in the GSE36001 dataset yielded 2345 DEGs, of which 1149 were upregulated and 1196 were downregulated in OS (Fig. 1E,F).

3.2 Functional Enrichment Analyses

A total of 23 candidate genes were obtained by overlapping the 2345 DEGs identified above with 2030 MRGs, 2660 IRGs, and 15,177 key module genes (Fig. 2A). These 23 candidate genes were significantly enriched in 293 GO

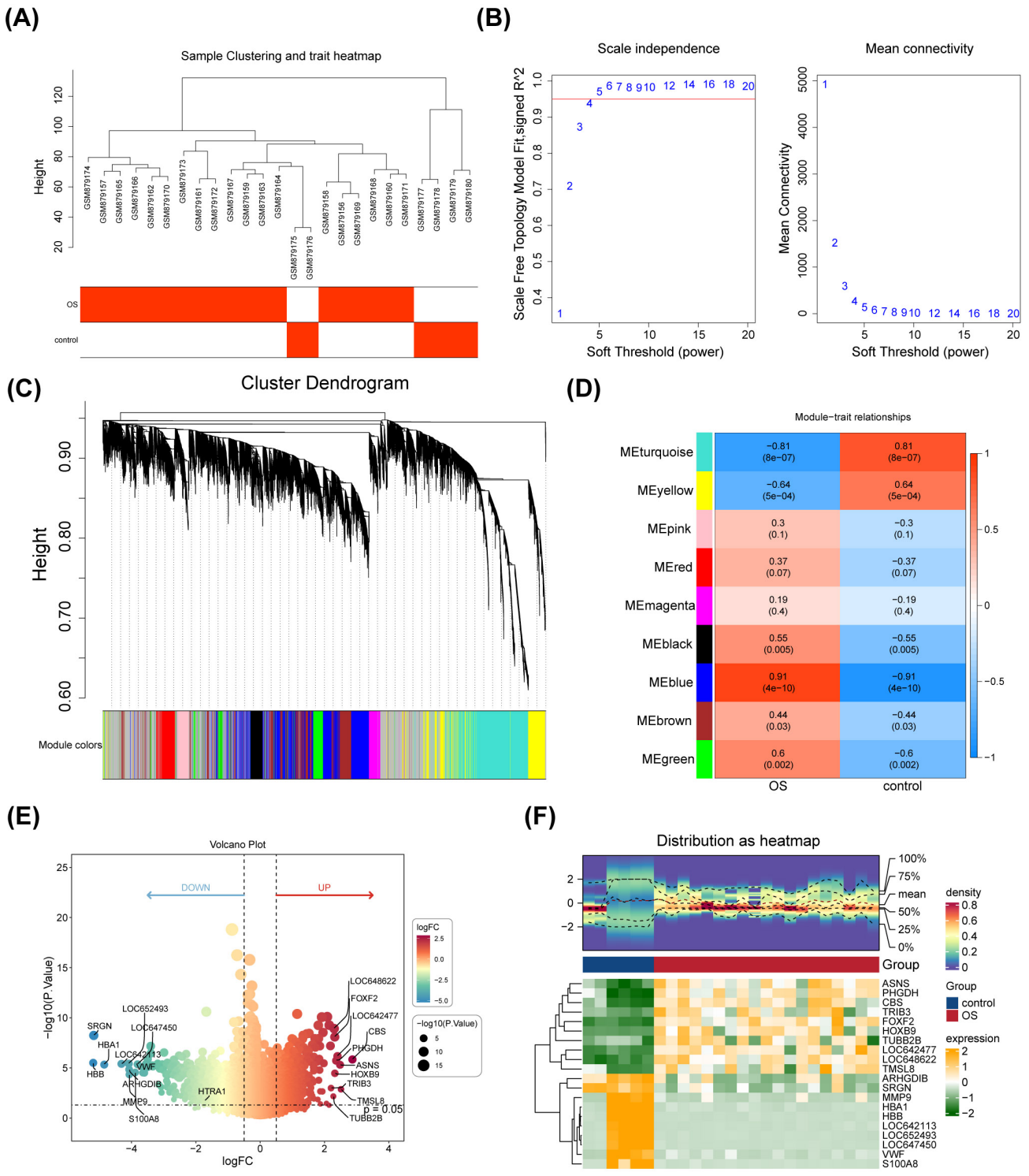

Fig. 1. WGCNA identifies module genes associated with phenotypes. (A) Hierarchical clustering of samples. The branches of the clustering tree represent individual samples, and the vertical coordinate represents the Euclidean distance between the sample and its centroid. (B) The selection of the soft threshold. The horizontal axis represents the weight parameter power, and the left graph's vertical axis represents the scale-free fit index. (C) The identification of co-expression modules. The upper part of the figure is a hierarchical clustering tree for genes, whereas the lower part is the gene module, also known as the network module. (D) The heatmap of correlations between modules and traits. (E) Differential expression gene volcano plot. The Y-axis represents −log10 (*p*-value), and the X-axis represents $\log_2$FC. (F) Heatmap of the differential gene density. Red represents high expression, and blue represents low expression. WGCNA, Weighted Gene Co-Expression Network Analysis.

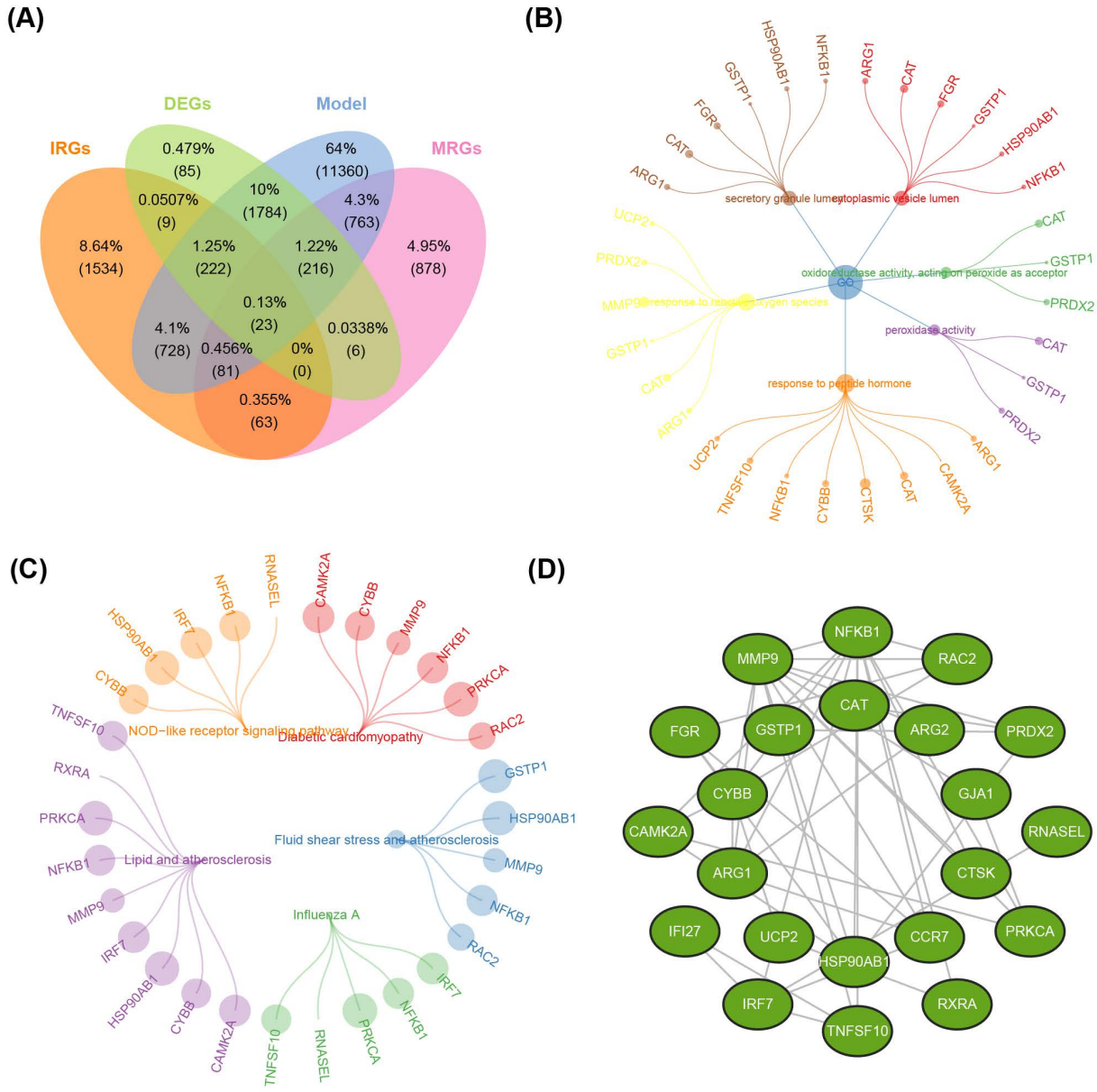

Fig. 2. Determination and functional enrichment analysis of candidate genes. (A) Key module genes, DEGs, MRGs, and IRGs were intersected to identify candidate genes. (B) GO enrichment analysis results for 23 candidate genes. (C) KEGG enrichment analysis results for 23 candidate genes. (D) PPI map of candidate genes. DEGs, differentially expressed genes; MRGs, mitochondria-related genes; IRGs, immune-related genes; GO, Gene Ontology; KEGG, Kyoto Encyclopedia of Genes and Genomes; PPI, Protein–Protein Interaction.

terms (269 biological process [BP], 19 cellular component [CC], and 5 molecular function [MF] terms) and 83 KEGG pathways. These enriched GO terms included embryonic organ development, renal system development, and embryonic organ morphogenesis (Fig. 2B). In addition, the enriched KEGG pathways included the NOD-like receptor signaling pathway, diabetic cardiomyopathy, and lipid and atherosclerosis (Fig. 2C). A PPI network consisting of these 23 candidate genes was composed of 23 nodes and 45 edges. Within this network, *HSP90AB1*, glutathione S-transferase Pi-1 (*GSTP1*), *CAMK2A*, and *NFKB1* exhibited the most interactions with the other candidate genes (Fig. 2D).

3.3 Construction of a Prognostic Risk Model

GSTP1, catalase (*CAT*), *TNFSF10*, and *PRKCA* were identified as prognostic genes through univariate Cox regression analysis (using $p < 0.2$ as the initial screening threshold), PH hypothesis testing, and LASSO regression analysis (Fig. 3A,B). The CIs for the four prognostic genes

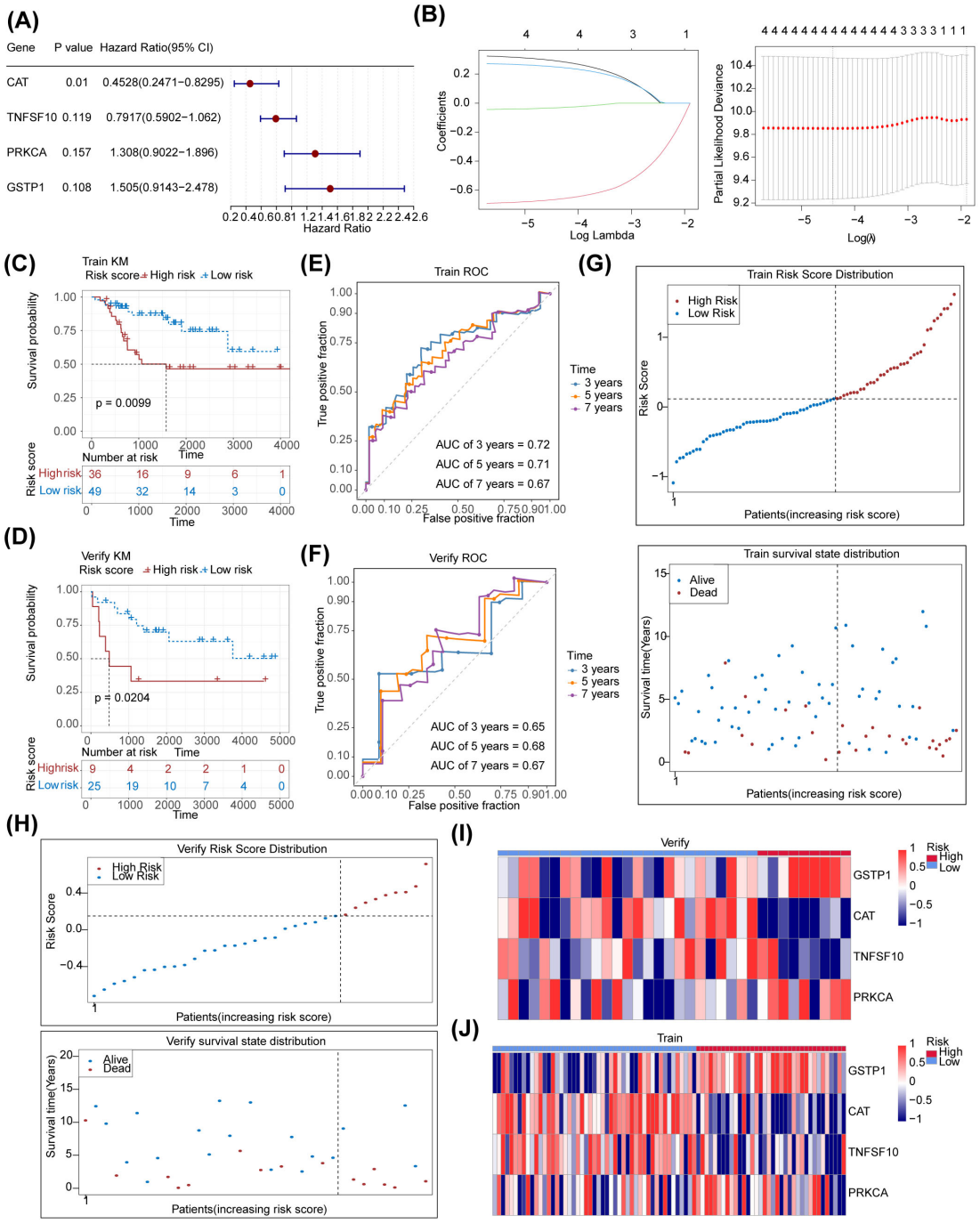

Fig. 3. Prognostic gene risk analysis. (A) Candidate genes associated with OS prognosis were identified using univariate Cox regression analysis. Hazard ratio (HR) >1, risk gene; HR <1, protective gene; HR = 1, irrelevant factor. (B) LASSO regression to further screen prognostic genes. Left: the horizontal axis represents the logarithm of lambda, and the vertical axis represents the variable coefficients. As lambda increases, the variable coefficients approach zero. When the optimal lambda is reached, the variables with coefficients equal to zero are excluded. Right: the horizontal axis is the logarithm of lambda, and the vertical axis is the model error. The optimal value of lambda is the minimum point of the red curve. (C) KM survival graph for patients with OS. (D) Survival curves of the high- and low-risk subgroups in the validation set. (E,F) Time-dependent ROC curves evaluating the prognostic model for 3-, 5-, and 7- year OS survival. (G,H) Risk curve and survival status. In the risk curve, red denotes high-risk samples, and blue denotes low-risk samples. Concerning the survival status, red denotes deceased patients, and blue denotes surviving patients. The dashed line denotes the median risk score. (I,J) Heatmap of prognostic gene expression. HRs with 95% CIs and log-rank *p* values are shown for Kaplan–Meier survival analyses. LASSO, least absolute shrinkage and selection operator; KM, Kaplan–Meier; OS, osteosarcoma; CIs, confidence intervals.

were as follows: *GSTP1* (HR = 1.505; 95% CI: 0.9143–2.478; $p = 0.108$), *CAT* (HR = 0.4528; 95% CI: 0.2471–0.8295; $p = 0.0103$), *TNFSF10* (HR = 0.7917; 95% CI: 0.5902–1.062; $p = 0.119$), and *PRKCA* (HR = 1.308; 95% CI: 0.9022–1.896; $p = 0.157$; **Supplementary Table 2**). A risk model was then developed using these four prognostic genes with the following formula: risk score = 0.29135304 × *GSTP1* expression + (−0.66319311) × *CAT* expression + (−0.03192373) × *TNFSF10* expression + 0.24954507 × *PRKCA* expression. Based on the optimal risk score cutoff, patients with OS were classified into high- and low-risk subgroups. In the TARGET-OS cohort, 85 patients with complete survival information were included, of whom 27 died during follow-up. After stratification based on the optimal risk score cutoff, the high-risk group included 36 patients, with 17 deaths and 19 survivors, whereas the low-risk group included 49 patients, with 10 deaths and 39 survivors. In the GSE16091 validation cohort, 34 patients were included, of whom 15 died during follow-up. The high-risk group included 9 patients, with 6 deaths and 3 survivors, while the low-risk group included 25 patients, with 9 deaths and 16 survivors (**Supplementary Table 3**). In the TARGET-OS cohort, KM analysis revealed that patients in the high-risk group had significantly poorer overall survival compared with those in the low-risk group (Fig. 3C). In the GSE16091 validation cohort, consistent with the results described above, the high-risk group had a poorer overall survival than the low-risk group (Fig. 3D). Moreover, ROC curve analysis demonstrated the ability of the risk model to accurately predict the 3-, 5-, and 7-year survival rates of patients with OS (Fig. 3E,F). Both the risk curve and scatter plot revealed an increase in the number of deaths with increasing risk scores (Fig. 3G,H). Heatmap analysis additionally revealed the overexpression of *GSTP1* and *PRKCA* in the high-risk subgroup, whereas *TNFSF10* and *CAT* were overexpressed in the low-risk subgroup (Fig. 3I,J).

Importantly, the bootstrap-corrected C-index values for both datasets were closely aligned with the original values, suggesting an absence of any significant model overfitting (**Supplementary Table 4**).

3.4 Establishment of a Nomogram With Strong Prognostic Performance in OS

Univariate Cox regression analysis revealed a significant association between risk score and overall survival in patients with OS (HR = 2.975, 95% CI: 1.580–5.602, $p < 0.001$; Fig. 4A). After adjusting for age, sex, and disease stage, multivariate Cox regression analysis indicated that the risk score remained an independent prognostic factor (HR = 2.608, 95% CI: 1.356–5.014, $p = 0.004$; Fig. 4B). Subsequently, a nomogram incorporating the expression of *GSTP1*, *CAT*, *TNFSF10*, and *PRKCA* was constructed to predict OS patient survival (Fig. 4C). In the calibration curve analysis, good consistency was observed between the predicted and reference values when predicting 3-, 5-, and 7-year survival, indicating that the predictive accuracy of the nomogram was high (Fig. 4D). DCA additionally revealed clear separation between the performance of the nomogram and the two extreme curves when predicting 3-, 5-, and 7-year survival, indicating that the nomogram had better predictive accuracy, with the overall predictive effect of the nomogram being higher than that of any single prognostic gene (Fig. 4E). Risk scores were further stratified according to clinical characteristics, including age, sex, and stage, revealing that these scores varied significantly with age, such that patients older than 14 years exhibited significantly lower risk scores for overall survival (Fig. 4F). KM survival curves revealed significant disparities between the two risk subgroups in terms of age (≤14 years vs. >14 years), sex (female vs. male), and metastasis status, with notably lower survival rates being observed for individuals in the high-risk group (**Supplementary Fig. 1**).

Furthermore, Model B exhibited a higher C-index (C-index = 0.8) compared with Model A (C-index = 0.73) (**Supplementary Fig. 2A**). ROC analysis additionally indicated that the AUC for Model B was superior to that of Model A when evaluating 3-, 5-, and 7-year overall survival (**Supplementary Fig. 2B,C**). DCA further confirmed that Model B provided a greater net benefit compared with Model A (**Supplementary Fig. 2D,E**). Overall, these results indicate that Model B has improved predictive ability.

3.5 Identification of Enriched Pathways Between the Two Risk Cohorts

Differential expression analysis identified 1390 DEGs when comparing the two risk cohorts, including 1098 upregulated and 292 downregulated genes in the high-risk cohort. Enrichment analysis revealed that these DEGs were enriched in 306 GO terms (138 BP, 88 CC, and 80 MF terms) and 16 KEGG pathways. The enriched biological functions and signaling pathways included renal system development, skeletal system morphogenesis, embryonic organ development, cytoskeleton in muscle cells, and neuroactive ligand–receptor interaction (Fig. 5A,B, **Supplementary Table 5**). GSEA further highlighted the enrichment of 23 signaling pathways. Among them, significant drug metabolism cytochrome P450, metabolism of xenobiotics by cytochrome P450, olfactory transduction, and starch and sucrose metabolism were enriched in the high-risk cohort, whereas viral myocarditis was enriched in the low-risk cohort (Fig. 5C, **Supplementary Table 6**). Furthermore, GSVA revealed 140 different biological functions based on the genes differentially expressed between the two risk cohorts, including the positive regulation of NF-κB transcription factor activity, interleukin 7-mediated signaling, and negative regulation of cAMP-mediated signaling pathways (Fig. 5D, **Supplementary Table 7**).

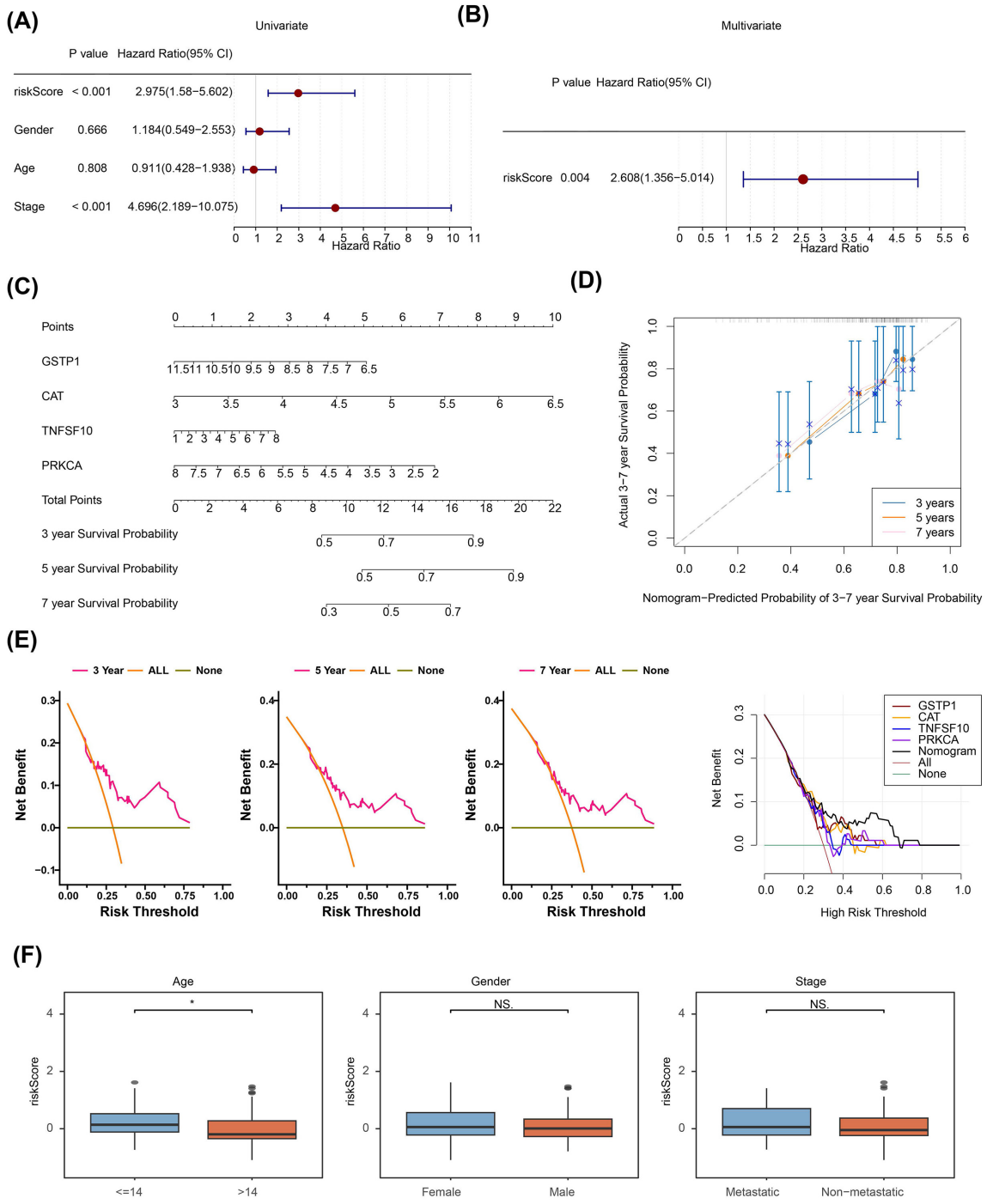

Fig. 4. The nomogram predicts the overall survival of patients with OS. (A) Forest plot of clinical indicators from univariate Cox regression. (B) Forest plot of clinical indicators from multivariate Cox regression. (C) Construction of a nomogram based on *GSTP1*, *CAT*, *TNFSF10*, and *PRKCA* for predicting the survival rate of patients. (D) Calibration curves assessing the predictive accuracy of the nomogram for 3-, 5-, and 7- year OS survival. (E) Decision curve analysis to assess the utility of prognostic genes for predicting outcomes. The horizontal axis represents the threshold probability, and the death risk probability of patient i is recorded as Pi. When Pi reaches a certain threshold (denoted as Pt), it is classified as positive, and an intervention measure is taken. Pi > Pt was judged as positive, and Pi < Pt was judged as negative. The vertical axis represents the net benefit rate after deducting costs from benefits. (F) Boxplot of risk score differences between patients with OS based on clinical features. Forest plots show HRs, 95% CIs, and *p* values from univariate and multivariate Cox regression analyses. *GSTP1*, Glutathione S-transferase Pi-1; *CAT*, catalase; *TNFSF10*, Tumor necrosis factor ligand superfamily member 10; *PRKCA*, protein kinase Cα; NS, not significant. * represents $p < 0.05$.

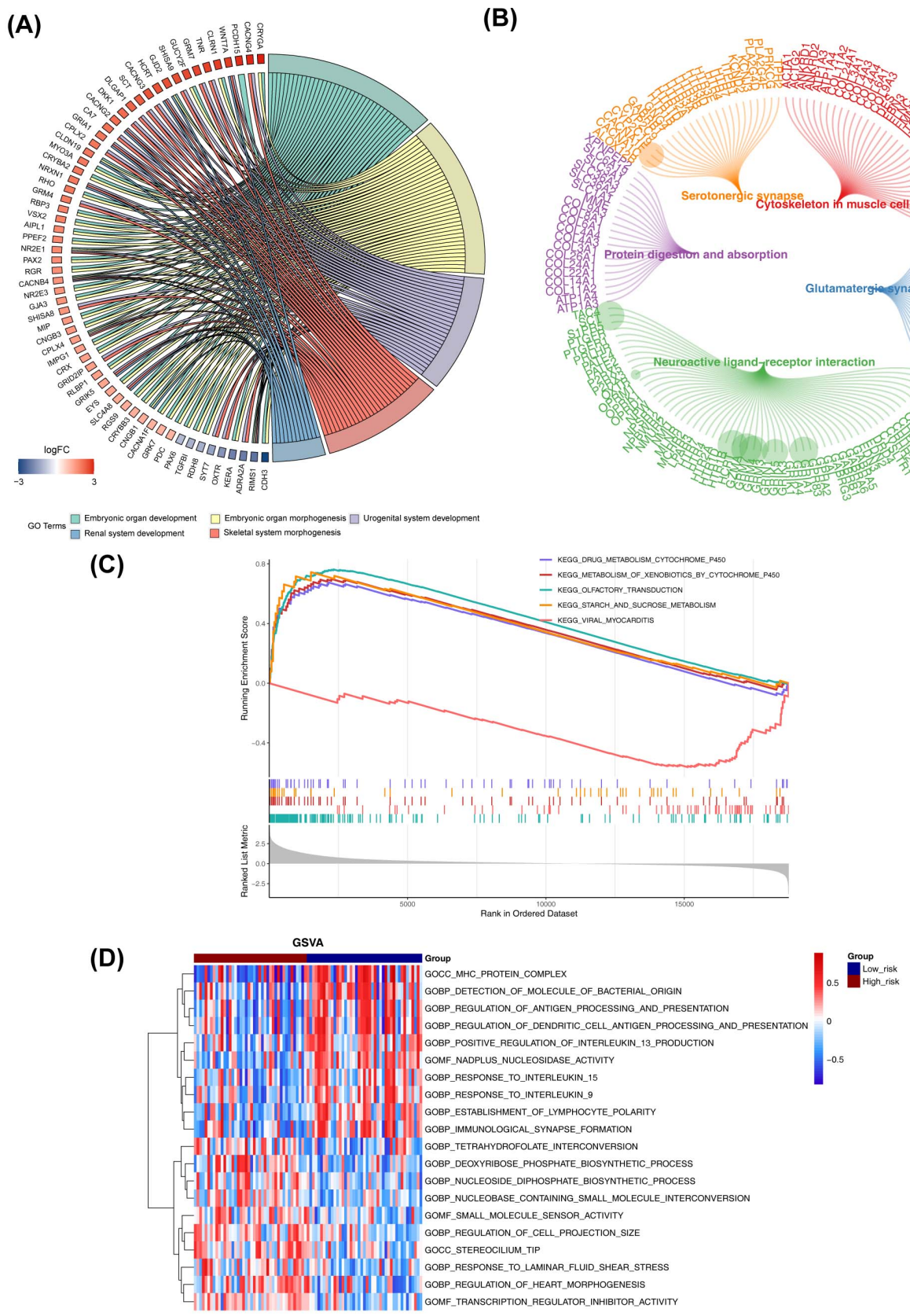

Fig. 5. Pathway enrichment in the two risk cohorts. (A,B) DEGs between the risk subgroups are enriched in various pathways. (C) GSEA reveals enriched pathways between the different risk groups. (D) GSVA analysis revealed differences in functional enrichment between the high- and low-risk groups. GSEA, Gene Set Enrichment Analysis; GSVA, Gene Set Variation Analysis.

3.6 Risk Subgroup-Related Differences in the Immune Microenvironment of OS

Using the ssGSEA algorithm, we next evaluated the immune microenvironment of OS patients, revealing differences in 14 immune cells and 8 immune checkpoints between the two risk subgroups (Fig. 6A,B). These differential immune cells included central memory $CD8^+$ T cells, effector memory $CD4^+$ T cells, natural killer T cells, natural killer cells, type 1 T helper cells, macrophages, plasmacytoid dendritic cells, effector memory $CD8^+$ T cells, central memory $CD4^+$ T cells, immature B cells, memory B cells, activated B cells, regulatory T cells (Tregs), and mast cells. The degree of immune cell infiltration for each of these populations was notably lower in the high-risk subgroup. With the exception of *TNFSF9*, analyzed immune checkpoint genes (*BTLA*, *CD200R1*, *CD27*, *CD274*, *CD28*, *TIGIT*, and *TNFSF14*) were expressed at significantly higher levels in the low-risk subgroup. The majority of these differential immune checkpoints were significantly positively correlated with *TNFSF10* (Fig. 6C). In addition, significant reductions in stromal, immune, and ESTIMATE scores were noted in the high-risk subgroup (Fig. 6D).

3.7 Drug Sensitivity Analyses

Drug sensitivity analyses were next conducted to explore the potential value of risk scores as a means of guiding chemotherapy. Correlation analyses indicated that 15 drugs, including elesclomol, gemcitabine, midostaurin, and shikonin, were significantly correlated with risk score (Fig. 7A, **Supplementary Table 8**). In addition, the IC_{50} values for these 15 drugs differed significantly between the two risk subgroups (Fig. 7B, **Supplementary Table 9**). Notably, the IC_{50} values of BIRB.0796, EHT.1864, elesclomol, OSI.906, PF.4708671, and *S*-trityl-L-cysteine were significantly higher in the high-risk subgroup. In contrast, the IC_{50} values of methotrexate, doxorubicin, and cisplatin, which are three commonly used chemotherapy drugs for the management of OS, did not differ between the risk subgroups.

A total of 103 and 118 miRNAs were obtained from the miRanda and miRDB databases, respectively. Five overlapping miRNAs were identified based on the overlap between these two databases: hsa-miR-190a-5p, hsa-miR-190b-5p, hsa-miR-589-5p, hsa-miR-3065-5p, and hsa-miR-581. In addition, eight lncRNAs were identified, including *XIST*, *AC021092.1*, *SNHG16*, *ADAMTSL4-AS1*, *AC016876.2*, *AC024267.1*, *KCNQ1OT1*, and *MALAT1*, all of which interact with hsa-miR-190a-5p and hsa-miR-589-5p. A total of 15 nodes and 13 interaction pairs were included in the constructed regulatory network, with *CAT* exhibiting a complex regulatory network (Fig. 7C). Together, these results offer a foundation for understanding the targeted regulation of prognostic genes.

3.8 Single-Cell Annotation of Cell Types in OS

Sample distributions in the GSE162454 dataset before and after quality control are shown in **Supplementary Fig. 3A,B**. In total, 2000 highly variable genes were screened in the single-cell dataset (**Supplementary Fig. 3C**), and the optimal number of principal components (PCs) was determined to be 20 based on dimensionality reduction (**Supplementary Fig. 3D**). Using these 20 PCs for clustering, we obtained 20 distinct cell clusters (Fig. 8A). PCA analysis did not reveal any distinct clusters among the samples, suggesting that there is no significant batch effect in the data (Fig. 8B). In total, 10 cell types were annotated, including osteoblastic OS cells, myeloid cells, T cells, CAFs, plasma cells, osteoclasts, endothelial cells, B cells, M1 macrophages, and M2 macrophages (Fig. 8C). Marker gene expression in these cell types was further evaluated (Fig. 8D). M1 macrophages were identified as a potentially relevant cell population based on patterns of *GSTP1*, *CAT*, *TNFSF10*, and *PRKCA* expression (Fig. 8E). Secondary clustering analysis further revealed that M1 macrophages could be characterized into five distinct subpopulations (**Supplementary Fig. 4**). Enrichment results also indicated that M1 macrophages were enriched in 1802 pathways, including the FMO oxidizes nucleophiles, lactose synthesis, and Cox reaction pathways (Fig. 8F).

3.9 Pseudotime and Cellular Communication Analyses of Key Cells

M1 macrophages differentiated into 13 different states, with differentiation typically starting in state 1 and primarily ending in state 11 (Fig. 9A,B). State 2 was skipped because there was no cell assignment. Later differentiation primarily occurred in M1 macrophage subclusters 1 and 2 (Fig. 9C). Subsequently, *CAT*, *PRKCA*, *GSTP1*, and *TNFSF10* were assigned to subclusters 1–4. Over the course of M1 macrophage differentiation, *CAT* and *PRKCA* expression initially decreased, then increased, followed by a final decrease, whereas *GSTP1* and *TNFSF10* expression first rose and then fell (Fig. 9D). Cellular communication results further highlighted strong and frequent interactions among all major cell types, with the exception of plasma cells, B cells, and T cells (Fig. 9E,F). Specifically, M1 macrophages were primarily associated with M2 macrophages, myeloid cells, and osteoclasts (Fig. 9G). In summary, these intercellular communication analysis results provide further support for the role of these cell populations in OS progression. Understanding these interactions may provide valuable guidance for pathologic studies of OS, offering a basis for new therapeutic interventions.

3.10 GSTP1, CAT, and PRKCA Expression Differs Significantly in OS

In the GSE36001 dataset, *GSTP1*, *CAT*, *TNFSF10*, and *PRKCA* expression levels were compared between the OS and control groups. *GSTP1*, *CAT*, and *PRKCA* expres-

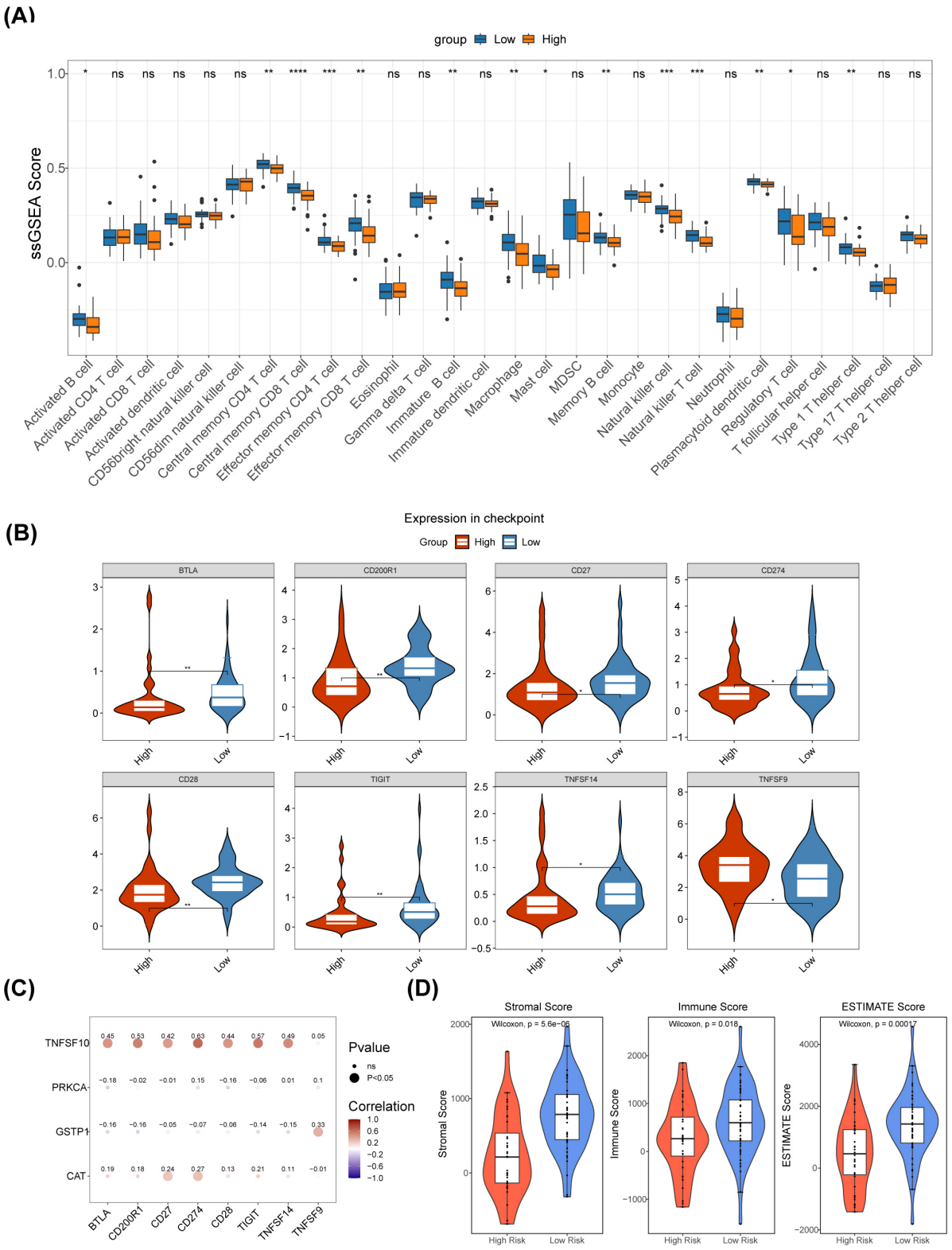

Fig. 6. The immune microenvironment exhibited significant differences between the two risk subgroups. (A,B) Differences in immune infiltration and immune checkpoint expression between the high- and low-risk groups. (C) Heatmap showing the correlation between differentially expressed immune checkpoint genes and prognostic genes. (D) Differences in stromal, immune, and ESTIMATE scores between the high- and low-risk OS subgroups. ns, not significant; *$p < 0.05$; **$p < 0.01$; ***$p < 0.001$; ****$p < 0.0001$.

sion significantly differed between the groups, with *CAT* exhibiting significantly higher expression levels in the control group, whereas *GSTP1* and *PRKCA* were expressed at significantly higher levels in the OS group (Fig. 10).

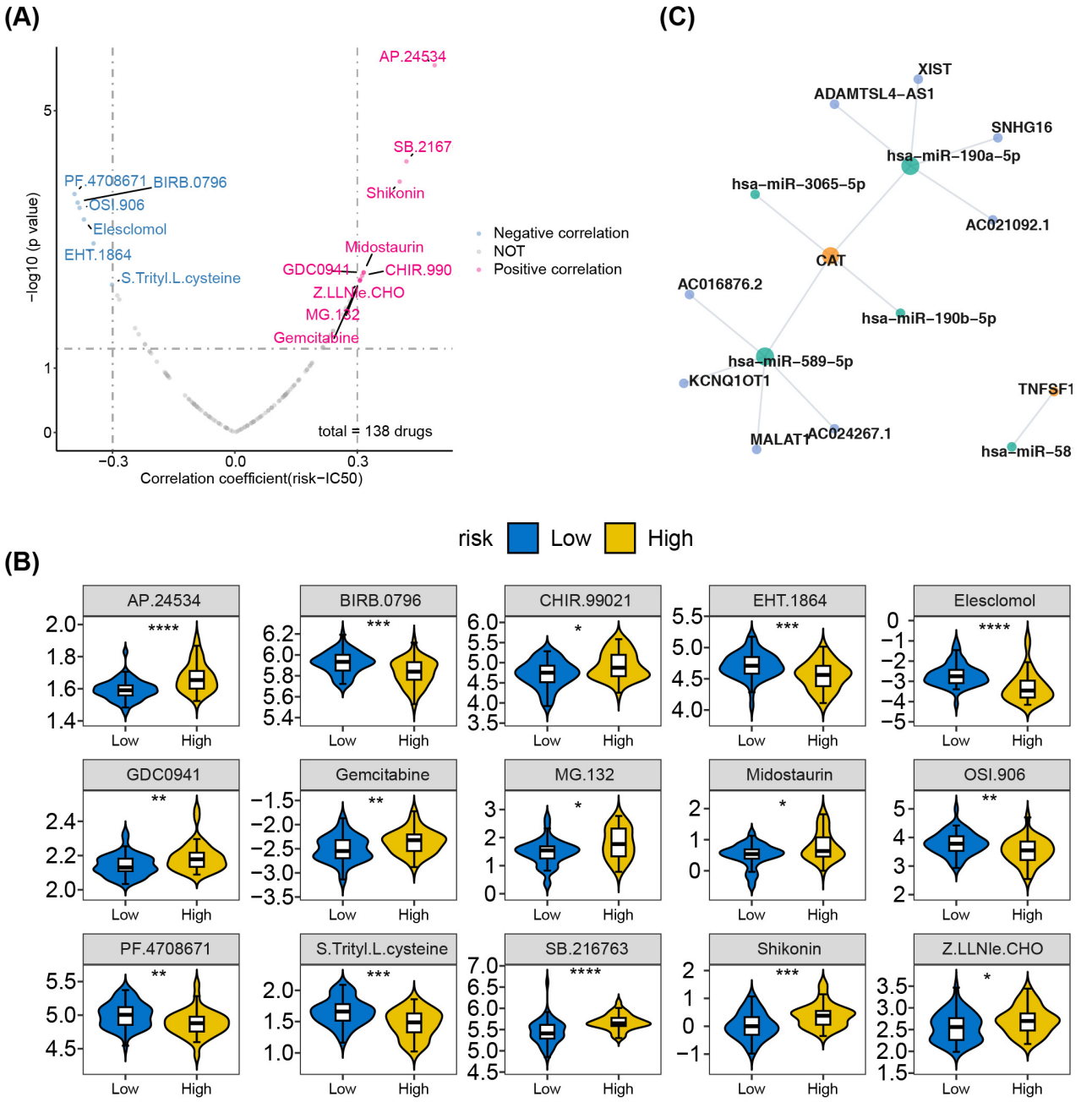

Fig. 7. The role of risk scores in guiding chemotherapy selection through drug sensitivity analysis. (A) Correlation analysis between drugs and risk scores. (B) Comparison of drug IC_{50} values between high- and low-risk groups. (C) lncRNA–miRNA–mRNA (prognostic gene) regulatory network. *$p < 0.05$; **$p < 0.01$; ***$p < 0.001$; ****$p < 0.0001$.

3.11 PRKCA Overexpression May Enhance the Proliferation, Migration, and Invasion of OS Cells

Based on a comprehensive analysis of differential gene expression in OS cell lines, we identified *PRKCA* as a key risk factor for OS, owing to its markedly altered expression. Previous studies have implicated *PRKCA* in various malignancies, including lung adenocarcinoma, oral tongue squamous cell carcinoma, neuroblastoma, and prostate cancer. However, relatively little of its role in OS is understood. As such, we conducted further functional experiments to examine the role of *PRKCA* in this cancer type.

Western blotting demonstrated the significant upregulation of PRKCA in OS cell lines (HOS and U2OS; Fig. 11A), and the transfection efficiency of *PRKCA* was further validated (Fig. 11B,C). RT-qPCR also confirmed this finding, demonstrating significantly higher *PRKCA* expression levels in HOS and U2OS cells as compared to normal osteoblasts (Fig. 11E,G). CCK-8 cell proliferation assays revealed that *PRKCA* overexpression significantly enhanced OS cell growth at 24, 48, and 72 h compared with control cells (Fig. 11D,F). In a wound healing assay, *PRKCA* overexpression enhanced the migration of OS cells

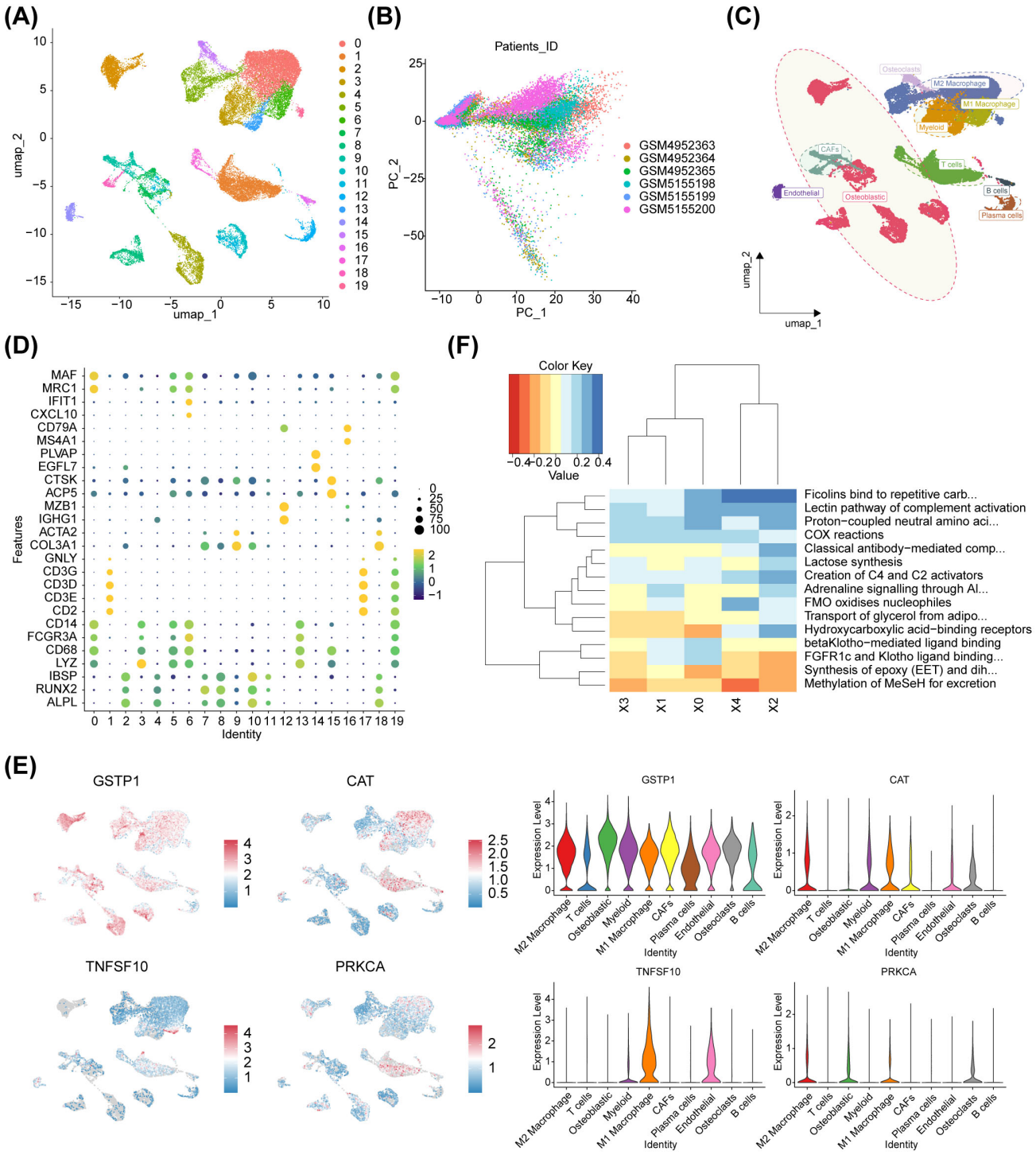

Fig. 8. Single-cell analysis of 10 cell types. (A,B) UMAP cluster diagram and PCA plot of highly variable genes. (C) Annotation of different cell types in the UMAP clustering chart. (D) Marker gene expression. (E) Different cell types have unique patterns of gene expression. (F) Enrichment analysis heatmap. UMAP, Uniform Manifold Approximation and Projection.

(Fig. 11H,I). Additionally, Transwell migration and invasion assays demonstrated that increased *PRKCA* expression notably promoted OS cell migratory and invasive activity (Fig. 11J,K). Collectively, these findings confirmed that *PRKCA* plays a critical role in promoting OS cell proliferation and migration.

3.12 PRKCA Silencing Significantly Inhibits OS Cell Proliferation, Migration, and Invasion

To more fully examine the functional importance of *PRKCA* in OS, we employed gene silencing technology to knock down *PRKCA* in HOS and U2OS cells, as confirmed by western blotting (Fig. 12A,B). Consistent with

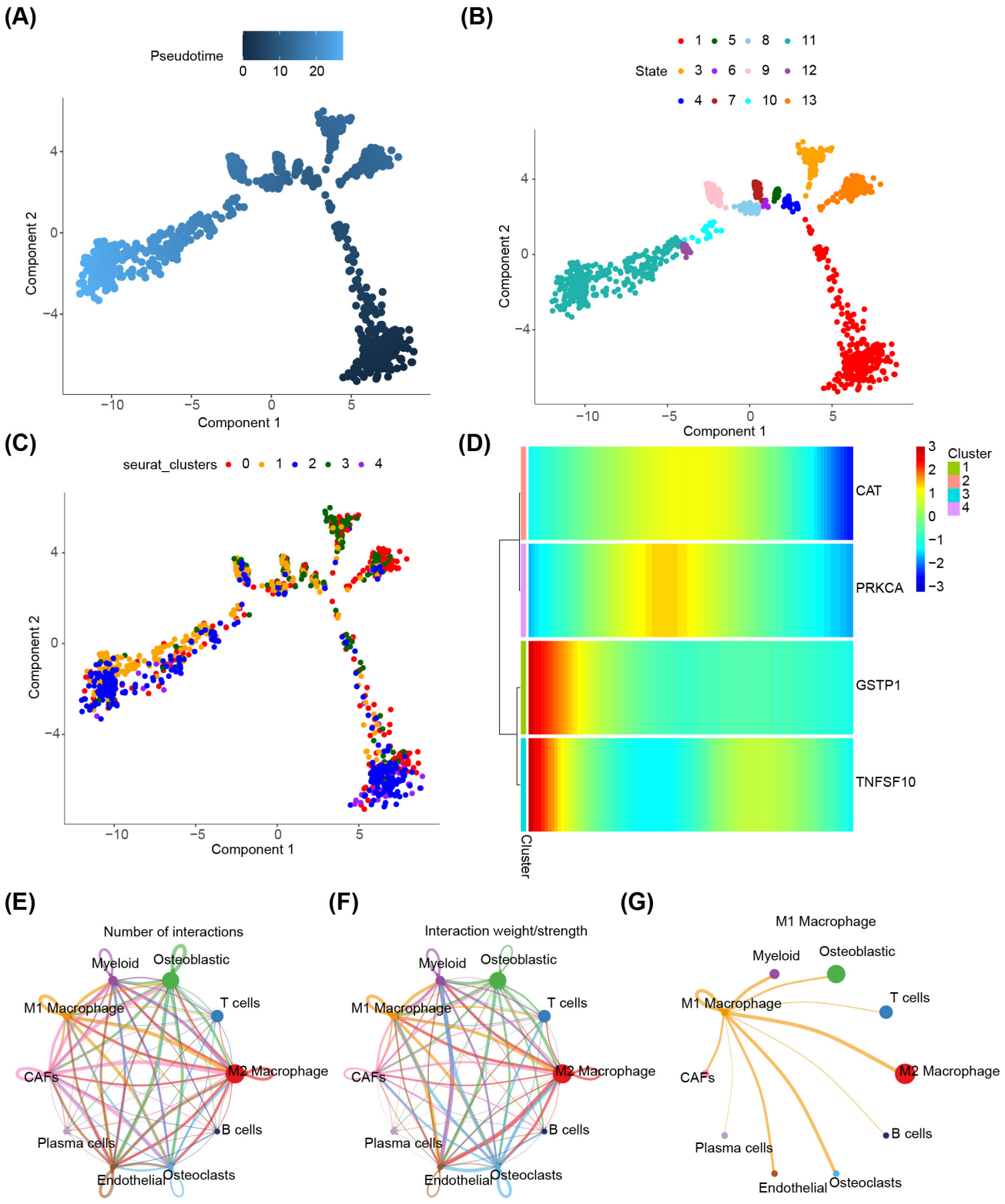

Fig. 9. Pseudotime trajectory analysis and cell communication network analysis of M1 macrophages. (A–C) Monocle analyses reveal the pseudotime trajectory plots of M1 macrophages (A), trajectory plots of different differentiation trajectory stages (B), and trajectory plots of different cell subpopulations (C). (D) Dynamic heatmap visualization of prognostic gene expression profiles. (E–G) M1 macrophages communicate with various cell types, as illustrated in the diagram of cell communication and interaction networks (E,F) and diagram of the individual effects of cell communication frequency (G).

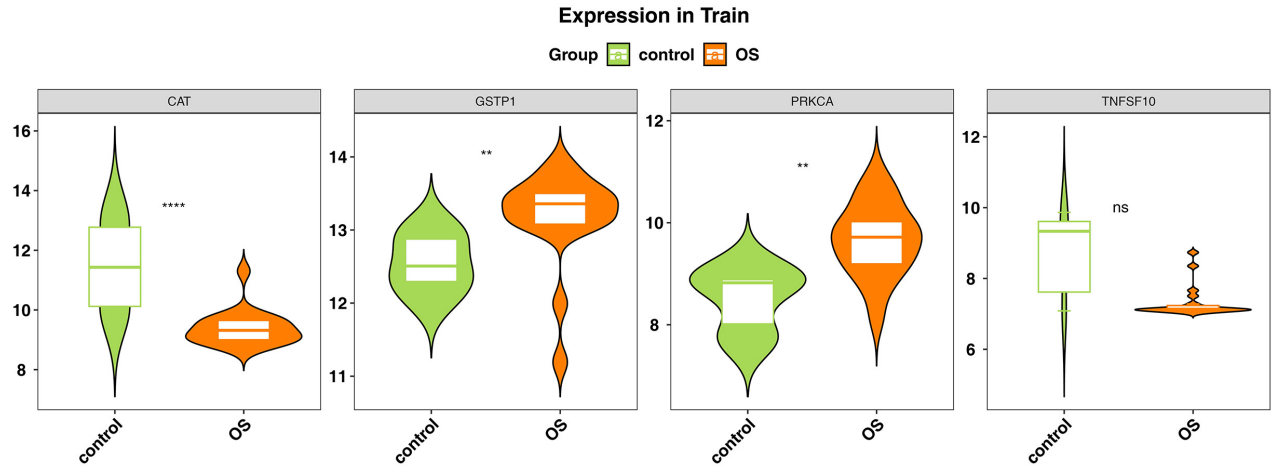

Fig. 10. The expression status of prognostic genes in OS tumor samples and normal control samples. ns, not significant; $^{**}p < 0.01$; $^{****}p < 0.0001$.

our hypothesis, RT-qPCR (Fig. 12D,F), CCK-8 assays (Fig. 12C,E), wound healing assays (Fig. 12G,H), and Transwell assays (Fig. 12I,J) demonstrated that *PRKCA* silencing significantly reduced the proliferative activity, migratory potential, and invasive capacity of OS cells. These findings reinforce the significant role that *PRKCA* plays in these malignant processes.

4. Discussion

In this study, we established and conducted a preliminary evaluation of a mitochondria- and immunity-related prognostic signature for OS by integrating bulk transcriptomic profiling with single-cell transcriptomic analysis. The model showed robust prognostic performance across independent cohorts and led to the identification of *PRKCA* as a biologically relevant risk-associated gene that is associated with OS progression and immune microenvironment remodeling in this cancer type. Based on bioinformatic analysis, we identified four prognostic genes (*GSTP1*, *CAT*, *TNFSF10*, and *PRKCA*) related to mitochondrial function and immunity in OS. Our results further highlight the closely interconnected nature of mitochondrial dysfunction and immune microenvironment remodeling during OS progression. The identified prognostic genes are broadly involved in oxidative stress regulation, inflammatory signaling, and macrophage-associated immune responses, indicating coordinated mitochondrial–immune crosstalk within the tumor microenvironment. Notably, single-cell transcriptomic analysis identified M1 macrophages as a potentially relevant cell population in OS [39]. In light of the established role of macrophage polarization in the regulation of inflammatory responses, tumor invasion, and immune surveillance, our findings offer further support for the hypothesis that mitochondria-associated immune dysregulation may contribute to OS progression and immune evasion [16].

CAT encodes the catalase enzyme, which functions to decompose H_2O_2 into nontoxic substances, thereby playing an important role in maintaining redox balance within the body. Wang et al. [40] reported that arsenic trioxide can induce the apoptotic death of p53-null OS MG63 cells through *CAT* inhibition. Wang et al. [41] additionally determined that manganese single-atom nanozymes (Mn-SANs) can catalyze endogenous H_2O_2 in OS cells into O_2 through *CAT*-like activity, effectively mitigating intratumoral hypoxia and activating oxidase (OXD)-like catalysis responsible for converting O_2 to cytotoxic O_2. The results of our study align with previous findings, indicating that *CAT* expression may be a protective factor for OS. However, the specific molecular mechanism through which it impacts OS prognosis remains to be further investigated. *CAT* has been shown to modulate cellular redox status by scavenging extracellular H_2O_2 in the tumor microenvironment, thereby reducing intracellular ROS levels and promoting T cell activation and long-term immunological memory [42]. *CAT* may therefore enhance T cell functionality within the OS immune microenvironment by regulating H_2O_2 levels during immune responses. CAT can also influence other immune components of the immune signaling network within tumors. For example, CAT exhibits synergistic interactions with multiple components, including toll-like receptors (TLRs) [43]. TLR activation can initiate innate and adaptive immune responses and modulate antitumor activity, suggesting that CAT plays a significant role in regulating the tumor immune microenvironment [44]. These observations suggest that, in addition to contributing to intracellular antioxidant defenses, CAT may influence tumor immune evasion through neutrophil- and TLR-mediated signaling pathways. We also observed the upregulation of *CAT* during the mid-stage of M1 macrophage polarization. In pro-inflammatory M1 macrophages, *CAT* expression has been shown to be suppressed through an

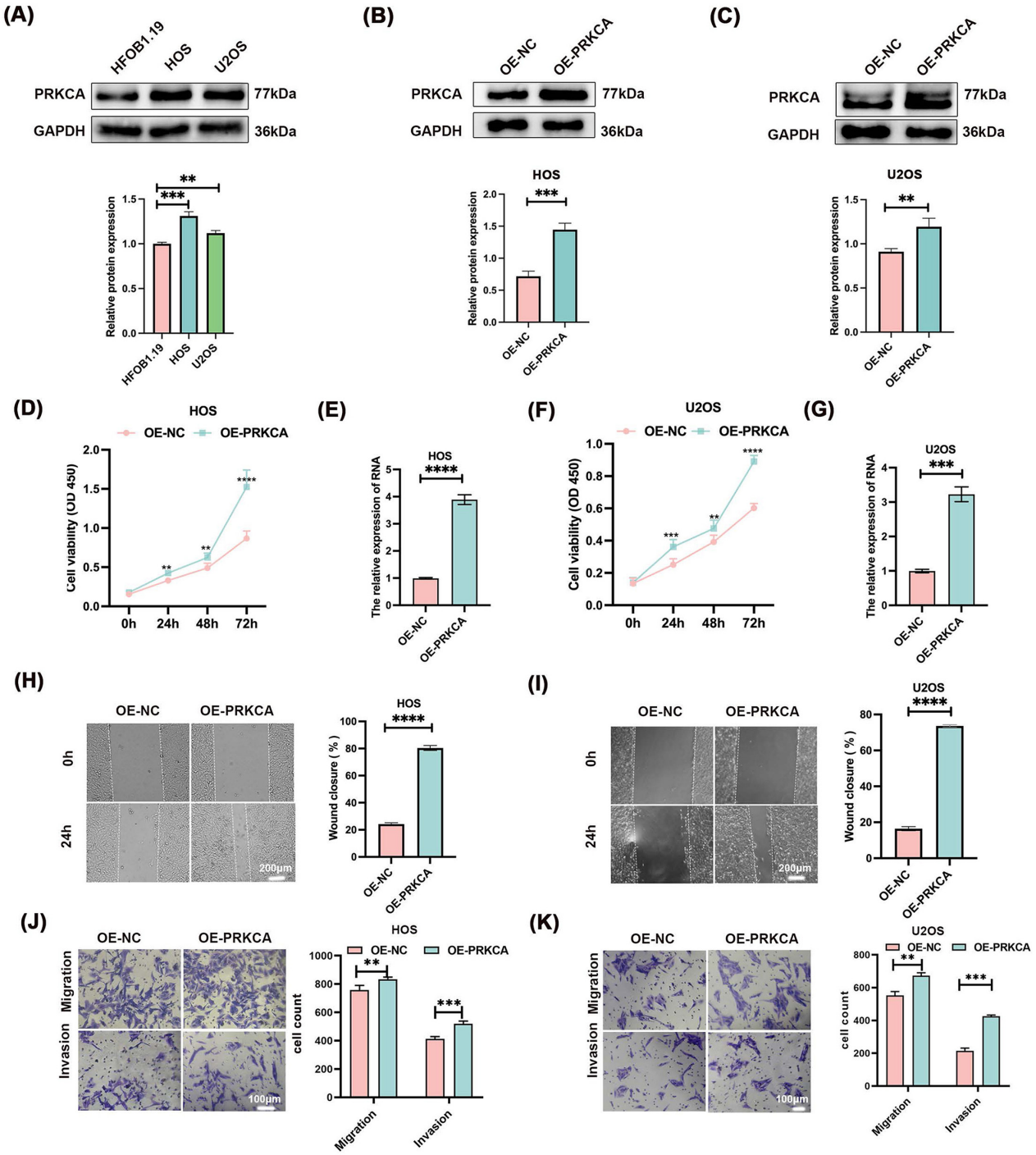

Fig. 11. The overexpression of *PRKCA* significantly enhanced the proliferation, migration, and invasion of both HOS and U2OS cells. (A–C) Western blotting. (D,F) CCK-8 assay. (E,G) RT-qPCR. (H,I) Wound-healing assay. Scale bar, 200 μm. (J,K) Transwell assay. Scale bar, 100 μm. CCK-8,Cell Counting Kit-8; RT-qPCR, reverse transcription quantitative polymerase chain reaction. $^{**}p < 0.01$; $^{***}p < 0.001$; $^{****}p < 0.0001$.

LSD1-dependent epigenetic mechanism, and its downregulation promotes M1 polarization and pro-inflammatory cytokine expression. Conversely, maintaining CAT levels can inhibit LPS-induced inflammatory responses. Taken together, these results suggest that stabilizing *CAT* expression through LSD1 inhibitors may mitigate M1-mediated pathological damage and potentially improve survival outcomes in OS [45], which is consistent with the results of the present study.

TNFSF10, also known as TNF-related apoptosis-inducing ligand (TRAIL) or CD253, belongs to the tumor necrosis factor superfamily. The protein encoded by *TN-*

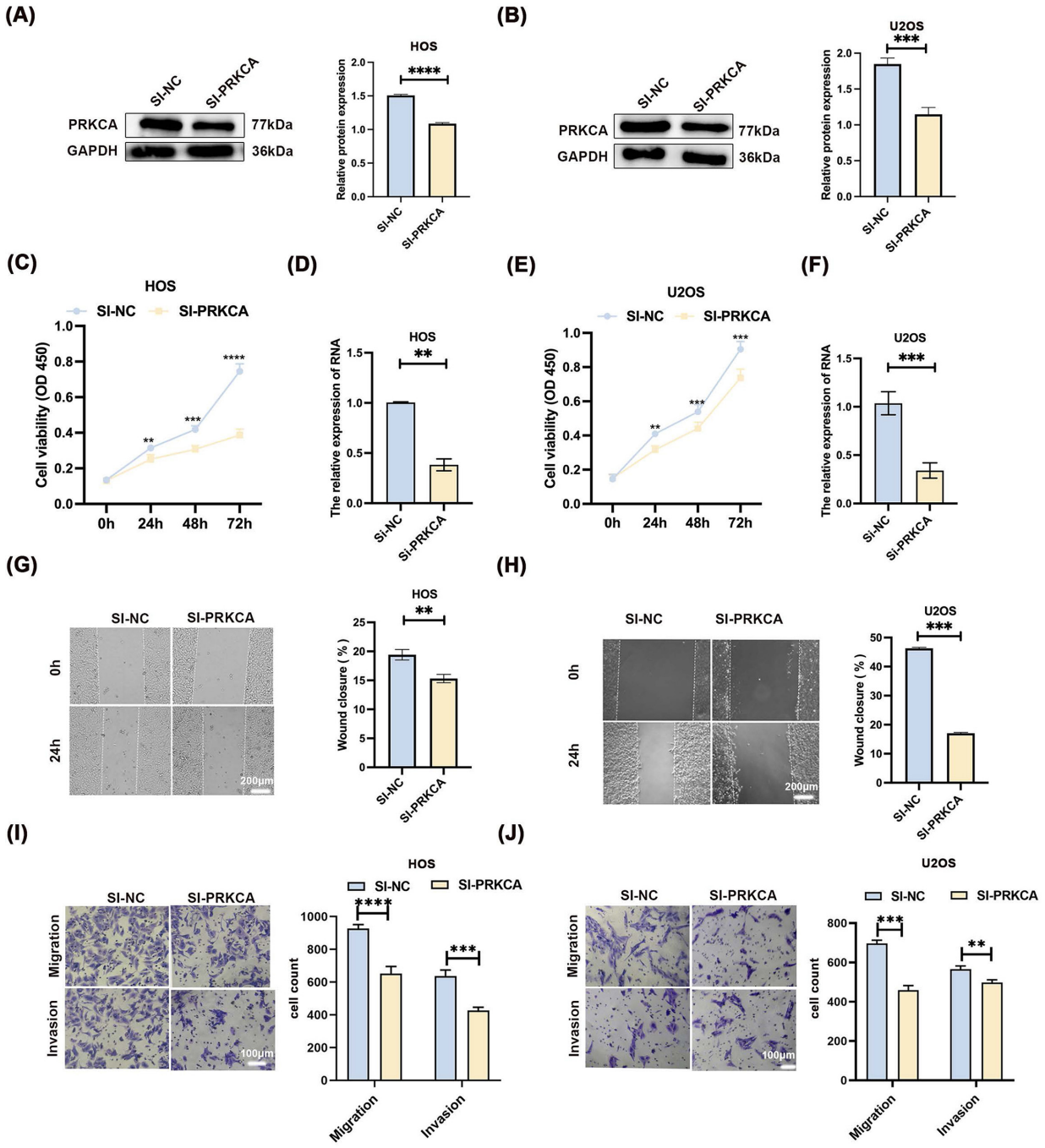

Fig. 12. Knockdown of *PRKCA* significantly reduced the proliferation, migration, and invasion of both HOS and U2OS cells. (A,B) Western blotting. (C,E) CCK-8 assay. (D,F) RT-qPCR. (G,H) Wound-healing assay. Scale bar, 200 μm. (I,J) Transwell assay. Scale bar, 100 μm. $^{**}p < 0.01$; $^{***}p < 0.001$; $^{****}p < 0.0001$.

FSF10 plays a crucial role in cellular processes, particularly in the regulation of apoptosis. Notaro et al. [46] reported that the WIN-dependent increase in SPARC levels plays a key role in OS cell TRAIL sensitivity. Disrupting mitochondrial Ca^{2+} homeostasis may offer a promising approach to overcoming TRAIL resistance in cancers while increasing tumor selectivity [47]. The present findings suggest that *TNFSF10* may be associated with OS prognosis. Furthermore, low levels of *TNFSF10* expression in skin cutaneous melanoma have been found to be significantly associated with aggressive clinicopathological features, diminished immune signaling activity, and reduced immune cell infiltration [48]. Consequently, the potential implications of *TNFSF10* for cancer prognosis and immunotherapy strategies merit further investigation. In addition to noting its functional roles in apoptosis and tumor immunity, we found that *TNFSF10* is highly expressed during the early stage of M1 macrophage polarization in OS. Previous stud-

ies have similarly identified *TNFSF10* as a risk-associated gene in prognostic models of pancreatic ductal adenocarcinoma, with higher expression levels being linked to poorer overall survival. Immune infiltration analysis further revealed that the high-risk group exhibited a marked reduction in M1 macrophage infiltration, concomitant with increased *TNFSF10* expression. This suggests that *TNFSF10* may contribute to the establishment of an immunosuppressive tumor microenvironment through its ability to suppress the antitumor activity of M1 macrophages, thereby promoting tumor progression and metastasis and ultimately reducing patient survival [49].

Among the identified prognostic genes, *PRKCA* was selected as the most biologically and clinically relevant candidate. Functional experiments revealed that *PRKCA* overexpression led to the significant enhancement of OS cell proliferation, migration, and invasion, whereas *PRKCA* silencing had the opposite effect. Previous studies have implicated *PRKCA* in tumor progression, adverse prognostic outcomes, and immune regulation across several malignancies, including lung adenocarcinoma, oral tongue squamous cell carcinoma, chordoid glioma, and colon cancer [50,51]. These results suggest that *PRKCA* participates in oncogenic signaling and the remodeling of the tumor microenvironment [52]. Combined with our single-cell findings, these results indicate that *PRKCA* may contribute to OS progression through mitochondria-associated immune regulatory mechanisms, emphasizing its potential as a therapeutic target. In light of these results, we developed a multivariate Cox regression model (Model B) incorporating four prognostic genes (*GSTP1*, *CAT*, *TNFSF10*, and *PRKCA*) along with clinical characteristics, which markedly enhanced the predictive performance of this model for outcomes in patients with OS. Compared with conventional prognostic indicators, this integrative model offers clinicians a more precise tool for assessing prognosis, thereby supporting more informed and optimized patient management.

In the high-risk subgroup, we observed decreased infiltration of central memory $CD8^+$ T cells, effector memory $CD8^+$ T cells, effector memory $CD4^+$ T cells, natural killer T cells, type 1 T helper cells, natural killer cells, activated B cells, and memory B cells, consistent with weakened immunity. The reduced infiltration of Tregs in the high-risk subgroup may be associated with the suppression of the immune response. Additionally, the decreased infiltration of macrophages and plasmacytoid dendritic cells in the high-risk subgroup may be linked to a reduction in antigen-presenting capabilities. Together, the immune cell infiltration analysis results suggest that immune function was suppressed in the high-risk subgroup. The observed reductions in ESTIMATE, immune, and stromal scores in the high-risk subgroup are indicative of decreases in the number or function of immune cells in tumor tissue. This may reflect a decrease in structural support for tumor tissue, thereby facilitating immune evasion by tumor cells. However, immune infiltration and ESTIMATE results are based solely on bioinformatics analyses and have not been validated through experimental evidence, highlighting this as an important avenue for our future research.

We observed significant differences in the IC_{50} values of 15 drugs, including AP.24534, BIRB.0796, CHIR.99021, EHT.1864, elesclomol, GDC0941, gemcitabine, MG.132, midostaurin, OSI.906, PF.4708671, *S*-trityl-L-cysteine, SB.216763, shikonin, and Z.LLNle.CHO, when comparing the high- and low-risk subgroups. Among these drugs, elesclomol is particularly noteworthy as a copper ionophore that regulates mitochondrial copper homeostasis and oxidative metabolism. In genetic models of copper deficiency, it can restore mitochondrial cytochrome c oxidase activity and respiratory function [53]. In tumor cells, elesclomol-induced oxidative stress is associated with mitochondrial metabolic reprogramming and can trigger cuproptosis. Although direct evidence linking elesclomol to the *PRKCA*/PKC-α pathway is currently lacking, there is prior evidence that it increases oxidative stress and enhances sensitivity to cytotoxic agents [54]. Further investigation into the mechanisms through which these drugs function will aid in the development of novel OS drugs, increasing the precision and personalization of OS treatment. The lack of significant differential efficacy for the common OS chemotherapeutic agents methotrexate, doxorubicin, and cisplatin when comparing the risk subgroups in this study may be attributable to their status as standard-of-care therapies. These agents elicit comparable therapeutic responses across most patients regardless of risk stratification, and their mechanisms of action are sufficiently robust to transcend variations in genetic risk profiles, resulting in minimal intergroup disparities in treatment outcomes. However, it is important to note that the drug sensitivity results from this study are solely based on bioinformatics analyses, which have limitations when attempting to directly translate IC_{50} values to patient outcomes. Variations in the tumor microenvironment, genomic characteristics, and physiological factors among individuals can affect drug sensitivity, potentially leading to discrepancies between predictions and actual clinical results. Therefore, careful evaluation is required before clinical application of these computational predictions, together with further experimental validation.

M1 macrophages were identified as a potentially relevant cell population in the OS microenvironment through single-cell transcriptomic analysis. As classically activated pro-inflammatory cells, M1 macrophages can exert direct antitumor effects in OS by releasing cytotoxic substances and pro-inflammatory factors, and they can enhance the immune response against tumors by activating T cells and other immune cells [55,56]. Richert et al. [39] demonstrated that TLR4 agonists induce OS regression through their ability to induce an antitumor immune response and reprogram M2 macrophages toward an M1 phenotype. The

results of this study are consistent with those of previous reports, suggesting that M1 macrophages play an important role in governing OS growth and development.

This study established a multidimensional comprehensive analysis framework for MRGs and IRGs in OS as a means of constructing a clinical outcome model with excellent predictive performance and a close association with immune activity and the efficacy of targeted therapy in patients with OS. In this study, bioinformatic analysis and RT-qPCR validation revealed that *PRKCA* expression was elevated in OS cells and negatively correlated with patient outcomes. This study investigated the role of *PRKCA* in OS cells. Overexpression of *PRKCA* markedly enhanced the invasive, migratory, and proliferative activities of OS cells. *PRKCA* knockdown experiments further confirmed its biological significance in OS. Collectively, these findings indicate that *PRKCA* is a promising therapeutic target for OS treatment. However, the functional roles of *GSTP1*, *CAT*, and *TNFSF10* in this study were inferred rather than experimentally validated. Future studies will focus on clarifying the roles of the remaining three genes.

5. Conclusion

In summary, this study established a mitochondria- and immunity-related prognostic risk signature for OS through integrated bulk transcriptomic and single-cell transcriptomic analyses. The resulting model exhibited favorable prognostic performance and was able to reveal potential associations between mitochondrial dysfunction, the remodeling of the immune microenvironment, and OS progression. *PRKCA* emerged as a key candidate among the identified prognostic genes, and *in vitro* experiments supported its role in promoting OS cell proliferation, migration, and invasion. Overall, these results provide insight into mitochondria–immune interactions in OS and may inform the development of prognostic stratification strategies and new targets for developing OS therapies.

6. Limitations

This study has several limitations that should be acknowledged. First, the small sample sizes of the derivation cohort (TARGET-OS, n = 88) and the validation cohort (GSE16091, n = 34) may limit the generalizability of our results and contribute to a higher risk of overfitting. The broader applicability of these results may also be constrained by cohort-specific biases related to treatment protocols and demographic characteristics. Therefore, future studies should include larger and more diverse populations to validate model performance. While our prognostic model showed favorable discriminative performance in the TARGET-OS and GSE16091 cohorts, and bootstrap-based internal validation suggested no evidence of overfitting, cutoff optimization may still have some bearing on the predictive performance of the model. Variations in risk stratification strategies or threshold selection may affect model robustness and stability across different populations. These considerations highlight the need for prospective validation in larger independent cohorts before this prognostic signature can be reliably translated into clinical practice. Moreover, our independent prognostic analysis was limited by the inaccessibility of key clinical data, including details on chemotherapy regimens, such that the incremental clinical utility of the model could not be fully evaluated in prospective cohorts. We were therefore unable to consider potential confounding factors that may have influenced model performance. Future studies should aim to compile a more comprehensive clinical dataset to support the further validation and refinement of our results. It should be noted that the relationship between the bulk-derived risk score and cell-type-specific activity remains inferential, and further integrated multi-omics analysis is required to validate these findings. Finally, while we demonstrated the prognostic utility of PRKCA expression, we were unable to establish a direct association between PRKCA expression levels and patient outcomes owing to a lack of clinical tissue chip and immunohistochemistry validation. Future studies should therefore focus on confirming these findings.

Availability of Data and Materials

The data used in this study are available from the corresponding author upon reasonable request. The GSE36001 (GPL6102), GSE16091 (GPL96), GSE162454 (GPL24676) datasets for this study can be found in the GEO (https://www.ncbi.nlm.nih.gov/gds) databases. The TARGET-OS dataset was obtained from the TARGET database (https://ocg.cancer.gov/programs/target). The TARGET-OS dataset was obtained from the database (https://www.broadinstitute.org/mitocarta/mitocarta30-inventory-mammalian-mitochondrial-proteins-and-pathways). Mitochondria-associated data originates from the GSEA database.

Author Contributions

JA, ZP, PX and XC designed the main research scheme. JZ, GY, JY and XM were responsible for data analysis and interpretation. PX, JY and JA wrote the paper. JA and XC performed multiple revisions and proofreading of the paper. All authors contributed to editorial changes in the manuscript. All authors read and approved the final manuscript. All authors have participated sufficiently in the work and agreed to be accountable for all aspects of the work.

Ethics Approval and Consent to Participate

Not applicable.

Acknowledgment

We would like to thank MJ Editor for providing English editing services during the preparation of this manuscript.

Funding

This research received no external funding.

Conflicts of Interest

The authors declare no conflicts of interest.

Supplementary Material

Supplementary material associated with this article can be found, in the online version, at https://doi.org/10.31083/FBL51093.

References

[1] Eaton BR, Schwarz R, Vatner R, Yeh B, Claude L, Indelicato DJ, et al. Osteosarcoma. Pediatric Blood & Cancer. 2021; 68: e28352. https://doi.org/10.1002/pbc.28352

[2] Gill J, Gorlick R. Advancing therapy for osteosarcoma. Nature Reviews. Clinical Oncology. 2021; 18: 609–624. https://doi.org/10.1038/s41571-021-00519-8

[3] Pu F, Guo H, Shi D, Chen F, Peng Y, Huang X, et al. The generation and use of animal models of osteosarcoma in cancer research. Genes & Diseases. 2024; 11: 664–674. https://doi.org/10.1016/j.gendis.2022.12.021

[4] Meazza C, Bastoni S, Scanagatta P. What is the best clinical approach to recurrent/refractory osteosarcoma? Expert Review of Anticancer Therapy. 2020; 20: 415–428. https://doi.org/10.1080/14737140.2020.1760848

[5] Beird HC, Bielack SS, Flanagan AM, Gill J, Heymann D, Janeway KA, et al. Osteosarcoma. Nature Reviews. Disease Primers. 2022; 8: 77. https://doi.org/10.1038/s41572-022-00409-y

[6] Janeway KA, Grier HE. Sequelae of osteosarcoma medical therapy: a review of rare acute toxicities and late effects. The Lancet Oncology. 2010; 11: 670–678. https://doi.org/10.1016/S1470-2045(10)70062-0

[7] van de Luijtgaarden ACM, Kapusta L, Bellersen L, Bokkerink JPM, Kaal SEJ, Versleijen-Jonkers YHM, et al. High prevalence of late adverse events in malignant bone tumour survivors diagnosed at adult age. Netherlands Journal of Medicine. 2014; 72: 516–522.

[8] Pain P, Spinelli F, Gherardi G. Mitochondrial Cation Signalling in the Control of Inflammatory Processes. International Journal of Molecular Sciences. 2023; 24: 16724. https://doi.org/10.3390/ijms242316724

[9] Gu H, Yang K, Wu Q, Shen Z, Li X, Sun C. A link between protein acetylation and mitochondrial dynamics under energy metabolism: A comprehensive overview. Journal of Cellular Physiology. 2021; 236: 7926–7937. https://doi.org/10.1002/jcp.30461

[10] Toki S, Yoshimaru T, Matsushita Y, Aihara H, Ono M, Tsuneyama K, et al. The survival and proliferation of osteosarcoma cells are dependent on the mitochondrial BIG3-PHB2 complex formation. Cancer Science. 2021; 112: 4208–4219. https://doi.org/10.1111/cas.15099

[11] Lai HT, Naumova N, Marchais A, Gaspar N, Geoerger B, Brenner C. Insight into the interplay between mitochondria-regulated cell death and energetic metabolism in osteosarcoma. Frontiers in Cell and Developmental Biology. 2022; 10: 948097. https://doi.org/10.3389/fcell.2022.948097

[12] Pan R, Pan F, Zeng Z, Lei S, Yang Y, Yang Y, et al. A novel immune cell signature for predicting osteosarcoma prognosis and guiding therapy. Frontiers in Immunology. 2022; 13: 1017120. https://doi.org/10.3389/fimmu.2022.1017120

[13] Wang Z, Wang Z, Li B, Wang S, Chen T, Ye Z. Innate Immune Cells: A Potential and Promising Cell Population for Treating Osteosarcoma. Frontiers in Immunology. 2019; 10: 1114. https://doi.org/10.3389/fimmu.2019.01114

[14] Zhou Q, Xian M, Xiang S, Xiang D, Shao X, Wang J, et al. All-Trans Retinoic Acid Prevents Osteosarcoma Metastasis by Inhibiting M2 Polarization of Tumor-Associated Macrophages. Cancer Immunology Research. 2017; 5: 547–559. https://doi.org/10.1158/2326-6066.CIR-16-0259

[15] Mills EL, Kelly B, O'Neill LAJ. Mitochondria are the powerhouses of immunity. Nature Immunology. 2017; 18: 488–498. https://doi.org/10.1038/ni.3704

[16] Saha T, Dash C, Jayabalan R, Khiste S, Kulkarni A, Kurmi K, et al. Intercellular nanotubes mediate mitochondrial trafficking between cancer and immune cells. Nature Nanotechnology. 2022; 17: 98–106. https://doi.org/10.1038/s41565-021-01000-4

[17] Baldwin JG, Gattinoni L. Cancer cells hijack T-cell mitochondria. Nature Nanotechnology. 2022; 17: 3–4. https://doi.org/10.1038/s41565-021-01006-y

[18] Chang J, Wu H, Wu J, Liu M, Zhang W, Hu Y, et al. Constructing a novel mitochondrial-related gene signature for evaluating the tumor immune microenvironment and predicting survival in stomach adenocarcinoma. Journal of Translational Medicine. 2023; 21: 191. https://doi.org/10.1186/s12967-023-04033-6

[19] Sun JR, Kong CF, Qu XK, Sun AT, Zhao KP, Sun JH. An immune-related prognostic signature associated with immune landscape and therapeutic responses in gastric cancer. Aging. 2023; 15: 1074–1106. https://doi.org/10.18632/aging.204534

[20] Langfelder P, Horvath S. WGCNA: an R package for weighted correlation network analysis. BMC Bioinformatics. 2008; 9: 559. https://doi.org/10.1186/1471-2105-9-559

[21] Ritchie ME, Phipson B, Wu D, Hu Y, Law CW, Shi W, et al. limma powers differential expression analyses for RNA-sequencing and microarray studies. Nucleic Acids Research. 2015; 43: e47. https://doi.org/10.1093/nar/gkv007

[22] Gustavsson EK, Zhang D, Reynolds RH, Garcia-Ruiz S, Ryten M. ggtranscript: an R package for the visualization and interpretation of transcript isoforms using ggplot2. Bioinformatics. 2022; 38: 3844–3846. https://doi.org/10.1093/bioinformatics/btac409

[23] Gu Z, Eils R, Schlesner M. Complex heatmaps reveal patterns and correlations in multidimensional genomic data. Bioinformatics. 2016; 32: 2847–2849. https://doi.org/10.1093/bioinformatics/btw313

[24] Chen H, Boutros PC. VennDiagram: a package for the generation of highly customizable Venn and Euler diagrams in R. BMC Bioinformatics. 2011; 12: 35. https://doi.org/10.1186/1471-2105-12-35

[25] Wu T, Hu E, Xu S, Chen M, Guo P, Dai Z, et al. clusterProfiler 4.0: A universal enrichment tool for interpreting omics data. Innovation. 2021; 2: 100141. https://doi.org/10.1016/j.xinn.2021.100141

[26] Shannon P, Markiel A, Ozier O, Baliga NS, Wang JT, Ramage D, et al. Cytoscape: a software environment for integrated models of biomolecular interaction networks. Genome Research. 2003; 13: 2498–2504. https://doi.org/10.1101/gr.1239303

[27] Lei J, Qu T, Cha L, Tian L, Qiu F, Guo W, et al. Clinicopathological characteristics of pheochromocytoma/paraganglioma and screening of prognostic markers. Journal of Surgical Oncology. 2023; 128: 510–518. https://doi.org/10.1002/jso.27358

[28] Liu TT, Li R, Huo C, Li JP, Yao J, Ji XL, et al. Identification of CDK2-Related Immune Forecast Model and ceRNA in Lung Adenocarcinoma, a Pan-Cancer Analysis. Frontiers in Cell and Developmental Biology. 2021; 9: 682002. https://doi.org/10.3389/fcell.2021.682002

[29] Heagerty PJ, Lumley T, Pepe MS. Time-dependent ROC curves for censored survival data and a diagnostic marker. Biometrics.

2000; 56: 337–344. https://doi.org/10.1111/j.0006-341x.2000.00337.x
[30] Hänzelmann S, Castelo R, Guinney J. GSVA: gene set variation analysis for microarray and RNA-seq data. BMC Bioinformatics. 2013; 14: 7. https://doi.org/10.1186/1471-2105-14-7
[31] Zhang X, Zhang X, Li G, Hao Y, Liu L, Zhang L, et al. A Novel Necroptosis-Associated lncRNA Signature Can Impact the Immune Status and Predict the Outcome of Breast Cancer. Journal of Immunology Research. 2022; 2022: 3143511. https://doi.org/10.1155/2022/3143511
[32] Maeser D, Gruener RF, Huang RS. oncoPredict: an R package for predicting in vivo or cancer patient drug response and biomarkers from cell line screening data. Briefings in Bioinformatics. 2021; 22: bbab260. https://doi.org/10.1093/bib/bbab260
[33] Robles-Jimenez LE, Aranda-Aguirre E, Castelan-Ortega OA, Shettino-Bermudez BS, Ortiz-Salinas R, Miranda M, et al. Worldwide Traceability of Antibiotic Residues from Livestock in Wastewater and Soil: A Systematic Review. Animals. 2021; 12: 60. https://doi.org/10.3390/ani12010060
[34] Hao Y, Hao S, Andersen-Nissen E, Mauck WM, III, Zheng S, Butler A, et al. Integrated analysis of multimodal single-cell data. Cell. 2021; 184: 3573–3587.e29. https://doi.org/10.1016/j.cell.2021.04.048
[35] Wang H, Li J, Li X. Construction and validation of an oxidative-stress-related risk model for predicting the prognosis of osteosarcoma. Aging. 2023; 15: 4820–4843. https://doi.org/10.18632/aging.204764
[36] Griss J, Viteri G, Sidiropoulos K, Nguyen V, Fabregat A, Hermjakob H. ReactomeGSA - Efficient Multi-Omics Comparative Pathway Analysis. Molecular & Cellular Proteomics. 2020; 19: 2115–2125. https://doi.org/10.1074/mcp.TIR120.002155
[37] Trapnell C, Cacchiarelli D, Grimsby J, Pokharel P, Li S, Morse M, et al. The dynamics and regulators of cell fate decisions are revealed by pseudotemporal ordering of single cells. Nature Biotechnology. 2014; 32: 381–386. https://doi.org/10.1038/nbt.2859
[38] Luo J, Deng M, Zhang X, Sun X. ESICCC as a systematic computational framework for evaluation, selection, and integration of cell-cell communication inference methods. Genome Research. 2023; 33: 1788–1805. https://doi.org/10.1101/gr.278001.123
[39] Richert I, Berchard P, Abbes L, Novikov A, Chettab K, Vandermoeten A, et al. A TLR4 Agonist Induces Osteosarcoma Regression by Inducing an Antitumor Immune Response and Reprogramming M2 Macrophages to M1 Macrophages. Cancers. 2023; 15: 4635. https://doi.org/10.3390/cancers15184635
[40] Wang Y, Wei Y, Zhang H, Shi Y, Li Y, Li R. Arsenic trioxide induces apoptosis of p53 null osteosarcoma MG63 cells through the inhibition of catalase. Medical Oncology. 2012; 29: 1328–1334. https://doi.org/10.1007/s12032-011-9848-5
[41] Wang CS, Xue HB, Zhuang L, Sun HP, Zheng H, Wang S, et al. Developing Single-Atomic Manganese Nanozymes for Synergistic Mild Photothermal/Multienzymatic Therapy. ACS Omega. 2023; 8: 49289–49301. https://doi.org/10.1021/acsomega.3c07714
[42] Aksoylar HI, Patsoukis N. Treatment with Exogenously Added Catalase Alters CD8 T Cell Memory Differentiation and Function. Advanced Biology. 2023; 7: e2101320. https://doi.org/10.1002/adbi.202101320
[43] Tian Y, Zhao WY, Liu YR, Song WW, Lin QX, Gong YN, et al. Machine learning reveals CAT gene as a novel potential diagnostic and prognostic biomarker in non-small cell lung cancer. Discover Oncology. 2024; 15: 774. https://doi.org/10.1007/s12672-024-01670-1
[44] Cao LL, Kagan JC. Targeting innate immune pathways for cancer immunotherapy. Immunity. 2023; 56: 2206–2217. https://doi.org/10.1016/j.immuni.2023.07.018
[45] Sobczak M, Strachowska M, Gronkowska K, Karwaciak I, Pułaski Ł, Robaszkiewicz A. LSD1 Facilitates Pro-Inflammatory Polarization of Macrophages by Repressing Catalase. Cells. 2021; 10: 2465. https://doi.org/10.3390/cells10092465
[46] Notaro A, Sabella S, Pellerito O, Vento R, Calvaruso G, Giuliano M. The secreted protein acidic and rich in cysteine is a critical mediator of cell death program induced by WIN/TRAIL combined treatment in osteosarcoma cells. International Journal of Oncology. 2016; 48: 1039–1044. https://doi.org/10.3892/ijo.2015.3307
[47] Ohshima Y, Takata N, Suzuki-Karasaki M, Yoshida Y, Tokuhashi Y, Suzuki-Karasaki Y. Disrupting mitochondrial Ca2+ homeostasis causes tumor-selective TRAIL sensitization through mitochondrial network abnormalities. International Journal of Oncology. 2017; 51: 1146–1158. https://doi.org/10.3892/ijo.2017.4096
[48] Xue L, Zhang W, Ju Y, Xu X, Bo H, Zhong X, et al. TNFSF10, an autophagy related gene, was a prognostic and immune infiltration marker in skin cutaneous melanoma. Journal of Cancer. 2023; 14: 2417–2430. https://doi.org/10.7150/jca.86735
[49] Liu X, Ren B, Fang Y, Ren J, Wang X, Gu M, et al. Comprehensive analysis of bulk and single-cell transcriptomic data reveals a novel signature associated with endoplasmic reticulum stress, lipid metabolism, and liver metastasis in pancreatic cancer. Journal of Translational Medicine. 2024; 22: 393. https://doi.org/10.1186/s12967-024-05158-y
[50] Jiang H, Fu Q, Song X, Ge C, Li R, Li Z, et al. HDGF and PRKCA upregulation is associated with a poor prognosis in patients with lung adenocarcinoma. Oncology Letters. 2019; 18: 4936–4946. https://doi.org/10.3892/ol.2019.10812
[51] Parzefall T, Schnoell J, Monschein L, Foki E, Liu DT, Frohne A, et al. PRKCA Overexpression Is Frequent in Young Oral Tongue Squamous Cell Carcinoma Patients and Is Associated with Poor Prognosis. Cancers. 2021; 13: 2082. https://doi.org/10.3390/cancers13092082
[52] Rosenberg S, Simeonova I, Bielle F, Verreault M, Bance B, Le Roux I, et al. A recurrent point mutation in PRKCA is a hallmark of chordoid gliomas. Nature Communications. 2018; 9: 2371. https://doi.org/10.1038/s41467-018-04622-w
[53] Soma S, Latimer AJ, Chun H, Vicary AC, Timbalia SA, Boulet A, et al. Elesclomol restores mitochondrial function in genetic models of copper deficiency. Proceedings of the National Academy of Sciences of the United States of America. 2018; 115: 8161–8166. https://doi.org/10.1073/pnas.1806296115
[54] Monk BJ, Kauderer JT, Moxley KM, Bonebrake AJ, Dewdney SB, Secord AA, et al. A phase II evaluation of elesclomol sodium and weekly paclitaxel in the treatment of recurrent or persistent platinum-resistant ovarian, fallopian tube or primary peritoneal cancer: An NRG oncology/gynecologic oncology group study. Gynecologic Oncology. 2018; 151: 422–427. https://doi.org/10.1016/j.ygyno.2018.10.001
[55] Yuan R, Li J. Role of macrophages and their exosomes in orthopedic diseases. PeerJ. 2024; 12: e17146. https://doi.org/10.7717/peerj.17146
[56] Chen Q, Zheng Y, Chen X, Xing Y, Zhang J, Yan X, et al. Bacteria Synergized with PD-1 Blockade Enhance Positive Feedback Loop of Cancer Cells-M1 Macrophages-T Cells in Glioma. Advanced Science. 2024; 11: e2308124. https://doi.org/10.1002/advs.202308124